

A Self-Replicating Single-Shape Tiling Technique for the Design of Highly Modular Planar Phased Arrays - The Case of L-Shaped Rep-Tiles

N. Anselmi,⁽¹⁾ *Senior Member, IEEE*, L. Tosi,⁽¹⁾ P. Rocca,⁽¹⁾⁽²⁾ *Senior Member, IEEE*, G. Toso,⁽³⁾ *Senior Member, IEEE*, and A. Massa,⁽¹⁾⁽⁴⁾⁽⁵⁾ *Fellow, IEEE*

⁽¹⁾ *ELEDIA Research Center (ELEDIA@UniTN - University of Trento)*
DICAM - Department of Civil, Environmental, and Mechanical Engineering
Via Mesiano 77, 38123 Trento - Italy
E-mail: {nicola.anselmi, luca.tosi, paolo.rocca, andrea.massa}@unitn.it
Website: www.eledia.org/eledia-unitn

⁽²⁾ *ELEDIA Research Center (ELEDIA@XIDIAN - Xidian University)*
P.O. Box 191, No.2 South Tabai Road, 710071 Xi'an, Shaanxi Province - China
E-mail: paolo.rocca@xidian.edu.cn
Website: www.eledia.org/eledia-xidian

⁽³⁾ *European Space Agency (ESA - ESTEC)*
Antenna and Submillimeter Wave Section, Radio Frequency Payloads & Technology Division, 2200 AG Noordwijk - The Netherlands
E-mail: giovanni.toso@esa.int
Website: www.esa.int

⁽⁴⁾ *ELEDIA Research Center (ELEDIA@UESTC - UESTC)*
School of Electronic Engineering, Chengdu 611731 - China
E-mail: andrea.massa@uestc.edu.cn
Website: www.eledia.org/eledia-uestc

⁽⁵⁾ *ELEDIA Research Center (ELEDIA@TSINGHUA - Tsinghua University)*
30 Shuangqing Rd, 100084 Haidian, Beijing - China
E-mail: andrea.massa@tsinghua.edu.cn
Website: www.eledia.org/eledia-tsinghua

This work has been submitted to the IEEE for possible publication. Copyright may be transferred without notice, after which this version may no longer be accessible.

A Self-Replicating Single-Shape Tiling Technique for the Design of Highly Modular Planar Phased Arrays - The Case of *L*-Shaped Rep-Tiles

N. Anselmi, L. Tosi, P. Rocca, G. Toso, and A. Massa

Abstract

The design of irregular planar phased arrays (*PAs*) characterized by a highly-modular architecture is addressed. By exploiting the property of self-replicating tile shapes, also known as *rep-tiles*, the arising array layouts consist of tiles having different sizes, but equal shape, all being generated by assembling a finite number of smaller and congruent copies of a single elementary building-block. Towards this end, a deterministic optimization strategy is used so that the arising rep-tile arrangement of the planar *PA* is an optimal trade-off between complexity, costs, and fitting of user-defined requirements on the radiated power pattern, while guaranteeing the complete overlay of the array aperture. As a representative instance, such a synthesis method is applied to tile rectangular apertures with *L*-shaped tromino tiles. A set of representative results, concerned with ideal and real antenna models, as well, is reported for validation purposes, but also to point out the possibility/effectiveness of the proposed approach, unlike state-of-the-art tiling techniques, to reliably handle large-size array apertures.

Key words: Phased Array Antenna, Planar Array, Irregular Tiling, Rep-tiles.

1 Introduction

The interest towards innovative phased array antennas (*PAs*) and related technologies has constantly grown over the last years owing to many possible applications as, for instance, millimeter wave communications [1][2] and sensing [3], automotive [4] and drone [5] radars, directional heating systems [6], and microwave imaging [7][8] just to mention a few. The capability of quickly reconfiguring the radiation pattern and its features by controlling the amplitude and/or the phase coefficients of the excitations of the array elements makes *PAs* a very attractive and promising technology. However, regularly-spaced digital *PAs*, where the radiating elements are arranged on a uniform lattice and each element is equipped with an independent transmit/receive module (*TRM*) and a digital channel, are too expensive and complex for standard applications [9][10].

Unconventional architectures [11], such as thinned [12][13], sparse [14][15], and clustered [16]-[35] arrays, have been recently considered to yield a suitable compromise between performance and costs. In such a framework, tiled *PAs* (i.e., clustered *PAs* composed by one or few elementary building-blocks) are gaining more and more attention thanks to their modularity that makes the whole antenna system, including the feeding network and the base-band layer, easier to fabricate and to maintain as well as controllable with a reduced number of *TRMs* or digital channels by using a single output/input for all the radiating elements clustered in a tile [22]-[35].

Nevertheless, two main issues/needs arise when dealing with clustered *PA* structures. First, the clusters have to be large enough to allow one a non-negligible cost saving (i.e., reduction of *TRMs* or digital channels), while the whole clustered *PA* must still afford a desired radiation pattern. In addition, the tile shapes must permit the design of irregular clustering configurations, which are required to avoid periodic quantization errors that generally imply the presence of high secondary lobes and/or grating lobes in the radiated pattern [36]. To properly tackle these drawbacks, tiling methods using either single [22]-[30] or multiple [31]-[35] tile shapes have been proposed. The *PAs* design has been generally cast as the optimization of user-defined cost-function terms related to the desired pattern performance indexes (e.g., the sidelobe level, the beamwidth, and the directivity) or quantifying the mismatch with a reference mask by also guaranteeing a full coverage of the whole antenna aperture. For instance, optimization

techniques based on the height-function coding strategy [25][27][28], evolutionary algorithms [25][27][28][32], compressive-sensing [31][33], convex-relaxation programming [30], random approaches [35] as well as exhaustive search [24] have been successfully applied to tile a finite area (i.e., the array aperture) with pre-selected tile shapes. However, such design methods have been usually developed for specific tile geometries or they turn out to be computationally expensive when the cardinality of the tile alphabet is huge and/or large apertures are at hand.

This paper proposes a novel and alternative methodology for the design of tiled *PAs* featuring high modularity instead of exploiting multiple different-shape tiles. It is based on the use and related properties of the self-replicating tiles, also called *rep-tiles*, to perform the irregular clustering of the array aperture. More specifically, the aperture is tiled with tiles having different sizes, but equal shape, all being generated by assembling a finite number of smaller and congruent copies of a single elementary building-block. Towards this end, a deterministic optimization strategy is used so that the arising rep-tile arrangement of the planar *PA* is an optimal trade-off between complexity, costs, and fitting of user-defined requirements on the radiated power pattern, while guaranteeing the complete overlay of the array aperture. As a representative instance, such a synthesis method is applied to tile rectangular apertures with *L*-shaped tromino tiles.

To the best of the authors knowledge, the main novelties of the proposed technique over the state-of-the-art array tiling comprise (i) the exploitation of the concept of self-replicating tiles for the design of planar *PAs*; (ii) the development of a novel deterministic tiling method to exploit the rep-tiling property for synthesizing clustered arrays with an optimal trade-off between architecture complexity and the fulfilment of user-defined radiation targets; (iii) the theoretical analysis of the properties of *L*-shape tromino rep-tiles and their engineering exploitation for the application of the proposed tiling method.

The rest of the paper is organized as follows. The mathematical formulation of the design of highly-modular planar *PAs* with self-replicating tiles is reported in Sect. 2, while the proposed deterministic synthesis method is described in Sect. 3 and customized to *L*-shape tromino rep-tiles, as well. Section 4 is devoted to the numerical validation against both ideal and real antenna models including mutual-coupling effects, as well. Eventually, some conclusions and final

remarks are drawn (Sect. 5).

2 Mathematical Formulation

Let us consider a planar PA covering a rectangular aperture A and composed by $M \times N$ radiating elements arranged on a regular lattice with inter-element spacing d_x and d_y along the x - and y -axes, respectively (Fig. 1). The power pattern radiated in far field by such a PA is given by $\mathcal{P}(u, v) = |\mathbf{e}(u, v) \times \mathcal{A}(u, v)|^2$ where $\mathbf{e}(u, v)$ is the embedded/active element pattern [37], which is assumed, without loss of generality, but only for the sake of notation simplicity, identical for all antennas, while $\mathcal{A}(u, v)$ is the array factor that depends of the array architecture at hand as detailed in the following, u ($u \triangleq \sin \theta \cos \phi$) and v ($v \triangleq \sin \theta \sin \phi$) being the direction cosines ($0 [\text{deg}] \leq \theta \leq 90 [\text{deg}]$, $0 [\text{deg}] \leq \phi \leq 360 [\text{deg}]$).

The surface A is partitioned into Q ($Q < M \times N$) tiles, $\varsigma = \{\varsigma_q; q = 1, \dots, Q\}$, each belonging to the *rep-tile* [38][39] alphabet Σ (i.e., $\varsigma_q \in \Sigma$). More specifically, the alphabet Σ is composed by $B \times R$ elements (i.e., $\Sigma = \{\sigma^{(r,b)}; r = 1, \dots, R; b = 1, \dots, B\}$), B and R being the number of admissible rep-tile orientations/flips and the maximum rep-tile order/level, respectively.

Let the smallest building-block of the rep-tile alphabet Σ , namely the generating rep-tile of order $r = 1$ with b -th ($1 \leq b \leq B$) orientation, $\sigma^{(r,b)} \Big|_{r=1}$, be a cluster of $I^{(r)} \Big|_{r=1}$ radiating elements. The rep-tile element of Σ of order $(r + 1)$ -th ($r = 1, \dots, R - 1$) and orientation b -th ($1 \leq b \leq B$) is then yielded by the union of S tiles of the previous r -th ($r = 1, \dots, R - 1$) order

$$\sigma^{(r+1,b)} = \bigcup_{s=1}^S \sigma^{(r,b_s)} \quad (1)$$

where S is a function of the rep-tile geometry at hand [e.g., L -shape tromino $\rightarrow S = 4$ - Fig. 2(b)] [39], b_s ($1 \leq b_s \leq B$) is the orientation of the s -th ($s = 1, \dots, S$) generating tile of r -th order ($r = 1, \dots, R - 1$). Therefore, a larger tile is yielded by assembling a finite number of S smaller and congruent copies with its same shape, but rotated in one of B possible positions [40] [Fig. 2(b)].

Moreover, the number of array elements belonging to a rep-tile of r -th ($r = 2, \dots, R$) order is given by

$$I^{(r)} = S^{r-1} \times I^{(1)}, \quad (2)$$

thus the aperture A of the array turns out to be tiled by multiple tiles with different sizes, but all having the same (even if scaled) shape [e.g., L -shape - Fig. 2(a)].

The array elements grouped into the q -th ($q = 1, \dots, Q$) tile, ς_q , share a unique input/output port, which is connected to the feeding network through a common TRM and/or a digital channel that provides a controllable complex weight w_q (Fig. 1) of amplitude α_q and phase β_q (i.e., $w_q = \alpha_q e^{j\beta_q}$). Accordingly, the antenna array factor is given by

$$\mathcal{A}(u, v) = \sum_{q=1}^Q w_q \mathcal{S}_q^{(r,b)}(u, v) e^{jk(x_q u + y_q v)} \quad (3)$$

where (x_q, y_q) is the center of ς_q within the aperture A and k is the wavenumber ($k \triangleq \frac{2\pi}{\lambda}$), λ being the wavelength at the working frequency f . Moreover, $\mathcal{S}_q^{(r,b)}$ is the space factor of the q -th ($q = 1, \dots, Q$) tile whose expression is

$$\mathcal{S}_q^{(r,b)}(u, v) = \sum_{i=1}^{I_q^{(r)}} e^{jk(x_i^{(r,b)} u + y_i^{(r,b)} v)} \quad (4)$$

where $(x_i^{(r,b)}, y_i^{(r,b)})$ is the center of the i -th ($i = 1, \dots, I_q^{(r)}$) radiating element of the alphabet entry, namely $\sigma_q^{(r,b)} = \Phi\{\varsigma_q\}^{(1)}$ associated to ς_q ($\varsigma_q \in \Sigma$).

In order to define the array synthesis problem at hand, let us code the tiling configuration of the $M \times N$ elements into Q rep-tiles, $\varsigma = \{\varsigma_q; q = 1, \dots, Q\}$, with the clustering vector \mathbf{c} of dimension $M \times N$ whose (m, n) -th ($m = 1, \dots, M; n = 1, \dots, N$) entry, c_{mn} , is given by $c_{mn} = \delta_{c_{mn}q} q$ where $\delta_{c_{mn}q} = 1(0)$ if the (m, n) -th radiating element belongs (does not belong) to the q -th rep-tile, ς_q (Fig. 3). Moreover, the amplitude/phase coefficients of the Q -sized set of rep-tiles, $\varsigma = \{\varsigma_q; q = 1, \dots, Q\}$, coded into the tiling vector \mathbf{c} , are chosen according to the excitation matching strategy [16][17] as follows

⁽¹⁾The operator Φ is called ‘‘associative operator’’ since it defines the correspondence between the q -th tile and the corresponding letter $\sigma^{(r,b)}$ of the alphabet Σ (i.e., $\varsigma_q \in \Sigma$).

$$\alpha_q = \frac{1}{I_q^{(r)}} \sum_{m=1}^M \sum_{n=1}^N \alpha_{mn}^{ref} \delta_{cmnq} \quad (5)$$

and

$$\beta_q = \frac{1}{I_q^{(r)}} \sum_{m=1}^M \sum_{n=1}^N \beta_{mn}^{ref} \delta_{cmnq}. \quad (6)$$

Such a choice allows one to yield the optimal setup of the weights of the tiled array, \mathbf{w} ($\mathbf{w} = \{w_q; q = 1, \dots, Q\}$), in the least-square sense since they have the minimum distance with respect to the “reference” excitations, \mathbf{w}^{ref} ($\mathbf{w}^{ref} = \{w_{mn}^{ref}; m = 1, \dots, M, n = 1, \dots, N\}$), of a fully-populated array of size $M \times N$ with a dedicated *TRM* for each (m, n) -th array element ($w_{mn}^{ref} = \alpha_{mn}^{ref} e^{j\beta_{mn}^{ref}}$) to afford an optimal power pattern, $\mathcal{P}^{ref}(u, v)$, or to optimally approximate a user-defined power pattern mask, $\Psi(u, v)$ in the visible range $\Omega = \{(u, v) : u^2 + v^2 \leq 1\}$.

Accordingly, the *Rep-Tile Array (RTA) Synthesis Problem* can be formulated as follows

Given a planar *PA* of $M \times N$ radiating elements arranged on a rectangular lattice, determine the optimal clustering of the array elements, \mathbf{c}_{opt} , corresponding to the set of rep-tiles, $\mathfrak{S}_{opt} = \{\varsigma_q^{opt}; q = 1, \dots, Q^{opt}\}$, belonging to the alphabet Σ (i.e., $\varsigma_q^{opt} \in \Sigma$), and the sub-array weights, \mathbf{w}_{opt} ($\mathbf{w}_{opt} = \{w_q^{opt} = \alpha_q^{opt} e^{j\beta_q^{opt}}; q = 1, \dots, Q^{opt}\}$), according to (5)(6) so that Q^{opt} is the minimum number of rep-tiles covering the aperture A and the user-defined power upper mask $\Psi(u, v)$ is matched by minimizing the mask matching index

$$\Gamma(\mathbf{c}) = \frac{\int_{\Omega} [P(u, v; \mathbf{c}) - \Psi(u, v)] \times \mathcal{H}\{P(u, v; \mathbf{c}) - \Psi(u, v)\} dudv}{\int_{\Omega} \Psi(u, v) dudv} \quad (7)$$

(i.e., $\mathbf{c}_{opt} = \arg\{\min_{\mathbf{c}} [\Gamma(\mathbf{c})]\}$), $\mathcal{H}\{\cdot\}$ being the Heaviside function.

Such a design problem is addressed with an innovative deterministic strategy detailed in Sect. 3.

3 RTA Design Method (RTAM)

Under the hypothesis that the array aperture A is fully tileable with R -th level rep-tiles, the *RTAM* is implemented by means of the following procedural steps:

- **Step 1. Initial R -th Level Tiling** - Depending on the cardinality $T^{(R)}$ of the problem at hand, either apply the Algorithm-X [43][44] to generate the whole set of $T^{(R)}$ complete clusterings of A with R -th order rep-tiles only, $\{\hat{\mathbf{c}}_t; t = 1, \dots, T^{(R)}\}$ and select the optimal configuration $\hat{\mathbf{c}}_{opt}$ of \hat{Q} tiles ($\hat{Q} \triangleq \frac{M \times N}{I^{(R)}}$) as

$$\hat{\mathbf{c}}_{opt} = \arg \left\{ \min_{t=1, \dots, T^{(R)}} [\Gamma(\hat{\mathbf{c}}_t)] \right\}, \quad (8)$$

or increase the tile order (i.e., $R \leftarrow R + 1$) to reduce the cardinality of the solution space ($T^{(R+1)} < T^{(R)}$) if the aperture can be still fully partitioned, or exploit a global optimization method [22] to sample the $T^{(R)}$ -size solution space for retrieving the global optimum of the cost function $\Gamma(\hat{\mathbf{c}}_t)$, $\hat{\mathbf{c}}_{best}$, and set $\hat{\mathbf{c}}_{opt} = \hat{\mathbf{c}}_{best}$. Set the initial ($h = 0$, h being the iteration index) tiling configuration to that yielded in the *Step 1* ($\mathbf{c}^{(h)}|_{h=0} \leftarrow \hat{\mathbf{c}}_{opt}$) and composed by R -th order rep-tiles only, $\boldsymbol{\varsigma}^{(h)}|_{h=0} = \left\{ \boldsymbol{\varsigma}_q^{(h)}|_{h=0} = \boldsymbol{\sigma}_q^{(R,b)}; q = 1, \dots, Q^{(h)}|_{h=0} \right\}$, being $Q^{(h)}|_{h=0} = \hat{Q}$;

- **Step 2. Rep-Tiling Optimization** - Increase the iteration index ($h \leftarrow h + 1$), set the rep-tile level to $r = R$, and apply the following loop

- **Step 2.1. Rep-Tile Selection** - For each q -th ($q = 1, \dots, Q^{(h)}$) tile of the h -th clustering, $\mathbf{c}^{(h)}$, compute the *substitution tiling metric (STM)*

$$\xi_q^{(h)} = \sum_{m=1}^M \sum_{n=1}^N |\mathcal{R}\{w_{mn}^{ref} - w_q^{(h)}\} + j\mathcal{I}\{w_{mn}^{ref} - w_q^{(h)}\}| \delta_{c_{mn}q} \quad (9)$$

to quantify the mismatch between the reference, \mathbf{w}^{ref} , and the current, $\mathbf{w}^{(h)}$ ($\mathbf{w}^{(h)} = \{w_q^{(h)} = \alpha_q^{(h)} e^{j\beta_q^{(h)}}; q = 1, \dots, Q^{(h)}\}$) weight sets, $\mathcal{R}\{\cdot\}$ and $\mathcal{I}\{\cdot\}$ being the real part and the imaginary one, respectively. Among the $Q^{(h)}$ reptiles of $\boldsymbol{\varsigma}^{(h)}$ select the \hat{q} -th one of r -th ($2 \leq r \leq R$) order with maximum *STM* value, $\xi_q^{(h)}$,

$$\hat{q} = \arg \max_{q=1, \dots, Q^{(h)}} \left\{ \xi_q^{(h)} \mid \mathbb{R}\{\sigma_q^{(r,b)}\} \geq 2 \right\}, \quad (10)$$

$\mathbb{R}\{\cdot\}$ being the operator that returns the rep-tile order of its argument;

- **Step 2.2. Rep-Tile Split** - Subdivide the \hat{q} -th tile of the current array clustering, $\mathbf{c}^{(h)}$, into S smaller tiles of $(r - 1)$ -th order ($\sigma_{\hat{q}}^{(r,b)} = \bigcup_{s=1}^S \sigma_s^{(r-1,b_s)}$) to generate a new tiling, $\mathbf{c}^{(h+1)}$, of the aperture A into $Q^{(h+1)} = Q^{(h)} + (S - 1)$ tiles;
- **Step 2.4. Excitations Update** - Compute the amplitude, $\boldsymbol{\alpha}^{(h+1)} = \{\alpha_q^{(h+1)}; q = 1, \dots, Q^{(h+1)}\}$, and the phase, $\boldsymbol{\beta}^{(h+1)} = \{\beta_q^{(h+1)}; q = 1, \dots, Q^{(h+1)}\}$, coefficients of the $Q^{(h+1)}$ tiles of $\mathbf{c}^{(h+1)}$ according to (5) and (6), respectively;
- **Step 2.5. Convergence Check** - If the power pattern radiated by the tiled array, $\boldsymbol{\varsigma}^{(h+1)}$, perfectly fulfils the radiation mask [i.e., $\Gamma(\mathbf{c}^{(h+1)}) = 0$] or the current number of clusters, $Q^{(h+1)}$, exceeds the user-definer maximum, Q_{max} (i.e., $Q^{(h+1)} \geq Q_{max}$ subject to $Q_{max} \leq \frac{M \times N}{I^{(1)}}$), stop the procedure and set the convergence iteration H to the current one (i.e., $H = h + 1$) as well as the optimal tiling to the current rep-tiles arrangement, $\mathbf{c}_{opt} = \mathbf{c}^{(h+1)}$. Otherwise, update the iteration index ($h \leftarrow h + 1$) and go to Step 2.1.

It is worth noticing that, besides the convergence solution \mathbf{c}_{opt} , the iterative loop of *Step 2* gives at each h -th ($h = 1, \dots, H$) iteration a compromise solution between feeding network complexity (i.e., $Q \rightarrow$ number of *TRMs*) and fulfilment of the pattern-mask constraint [i.e., $\Gamma(\mathbf{c}^{(h+1)})$] so that finally a ‘‘Pareto’’ front of H layouts can be defined and profitably exploited by the array designer.

3.1 The Case of *L*-Shaped Rep-Tiles

The *RTAM* is customized hereinafter to *L*-tromino tiles, which are rep-tiles [38][39] with $I^{(r)} \Big|_{r=1} = 3$ and $S = 4$ [Fig. 2(a)], as a representative example of self-replicating tile geometries [Fig. 2(b)].

Tileability Theorem

The *RTAM* requires the fulfilment of the complete tileability of the array aperture A with the largest (i.e., highest order R) tiles of the alphabet Σ (i.e., $\{\sigma^{(R,b)}; b = 1, \dots, B\}$) since the highest order tiles can be certainly subdivided into smaller ones thanks to the self-replicating

property of the rep-tiles. The covering theorem for an exact (i.e., complete) rectangular tessellation with R -th order L -tromino tiles [45] reads as follows

L-tromino Covering Theorem - Let A a rectangular aperture of $M \times N$ elements/pixels, M and N being integer numbers such that $2 \times l^{(R)} \leq M \leq N$, where $l^{(R)} = \sqrt{\frac{l^{(R)}}{3}}$ is the side length of the R -th order L -tromino tile. Then, A can be fully covered with L -tromino tiles of order R if and only if one of the following conditions holds true

- $\widehat{M} = 3$ and \widehat{N} is even [e.g., Fig. 4(a)];
- $\widehat{M} \neq 3$ and $\lfloor \frac{M \times N}{l^{(R)}} \rfloor = 0$, $\lfloor \cdot \rfloor$ being the modulo operation [e.g., Fig. 4(c) and Fig. 4(e)]

where $\widehat{M} \triangleq \frac{M}{l^{(R)}}$ and $\widehat{N} = \frac{N}{l^{(R)}}$. Otherwise, A is not fully tileable with R -th order L -tromino tiles [e.g., Fig. 4(b), Fig. 4(d), and Fig. 4(f)].

Problem Cardinality

According to [46], the number of tilings, $T^{(R)}$, that exactly/fully cover an aperture A of $M \times N$ pixels/elements with R -th order L -trominoes is equal to

$$T^{(R)} = \widehat{g}_{po}]_{p=1}^{o=2^{\widehat{M}}} \quad (11)$$

where \widehat{g}_{po} is the (p, o) -th $(p, o = 1, \dots, 2^{\widehat{M}})$ entry of the matrix $(\mathbf{G}_{\widehat{M}})^{\widehat{N}-1}$, which is the square and symmetric matrix of size $2^{\widehat{M}} \times 2^{\widehat{M}}$ given in the *Appendix (5)*. In order to give an idea of the cardinality of the solution space of the tiling problem at hand, Table I gives the T values for some rectangular apertures with sizes $\{\widehat{M} \times \widehat{N} ; 2 \leq \widehat{M} \leq 9, 2 \leq \widehat{N} \leq 9\}$.

It is worth pointing out that *a-priori* knowing the value of $T^{(R)}$ (11) or, at least, its order of magnitude, is a very important information for the array designer since it enables the choice of an exhaustive enumerative strategy, which guarantees the retrieval of the optimal solution in the *Step 1* of the *RTAM* in Sect. 3 since evaluating all $T^{(R)}$ exact tiling configurations, or it forces to reformulate the problem as an optimization one when the cardinality of the solution space turns out prohibitive for an exhaustive search.

RTAM Customization

For illustrative purposes, let us consider the application of the *RTAM* ($H = 3$ iterations) to a planar array of $M \times N = 8 \times 16$ elements (Fig. 5) by using the alphabet Σ of L -tromino rep-tiles in Fig. 2(a) being $R = 3$ and $B = 4$.

Starting ($h = 0$) from the initial clustering of R -th order L -tromino tiles found at the *Step 1* (Sect. 3), $\hat{\mathbf{c}}_{opt}$, in Fig. 5(a) where the normalized values of the *STM* of the $Q^{(h)} \Big|_{h=0} = 4$ tiles (i.e., $\{\xi_q^{(h)}; q = 1, \dots, Q^{(h)}\}$) are indicated, as well, the $I^{(3)}$ -size ($I^{(R)} \Big|_{R=3} = 48$) tile with maximum *STM* (i.e., $\xi_2^{(1)} = 1.0$) [Fig. 5(a)] is chosen for division according to (10) of *Step 2.1* (i.e., $\hat{q} = 2$) to yield the new tiled arrangement $\mathbf{c}^{(1)}$ shown in Fig. 5(b) of $Q^{(1)} = 7$ rep-tiles, namely $Q_R^{(1)} = 3$ rep-tiles of order R , while $S = 4$ rep-tiles of order $R - 1$ ($Q_{R-1}^{(1)} = S$), being $Q^{(h)} = \sum_{r=1}^R Q_r^{(h)}$. Afterwards, other two tiles including $I^{(2)}$ ($I^{(2)} = 12$) [Fig. 5(c)] and $I^{(3)}$ [Fig. 5(e)] array elements are the candidates for division (10) at the iteration $h = 2$ and $h = H$, respectively, $\mathbf{c}^{(2)}$ of $Q^{(2)} = 10$ ($Q_R^{(2)} = Q_{R-1}^{(2)} = 3$ and $Q_{R-2}^{(2)} = S$) rep-tiles [Fig. 5(d)] and $\mathbf{c}^{(3)}$ of $Q^{(3)} = 13$ ($Q_R^{(3)} = 2$, $Q_{R-1}^{(3)} = 7$, and $Q_{R-2}^{(3)} = S$) rep-tiles [Fig. 5(f)] being the generated array clusterings.

4 Numerical Results

This section is devoted to the analysis of the behavior and the assessment of the performance of the proposed *RTAM*.

The first example deals with an array comprising $M \times N = 8 \times 12$ isotropic [i.e., $\mathbf{e}(u, v) = 1$] radiating elements with uniform half-wavelength ($d_x = d_y = \frac{\lambda}{2}$) inter-element spacing. The reference excitations have been computed with a Convex Programming (*CP*) based approach [47] to fit the upper-bound power mask $\Psi(u, v)$ in Fig. 6(a), which is centered in $(u_0, v_0) = (0, 0)$ and it is characterized by a rectangular mainlobe region of dimensions $BW_u = 0.50$ and $BW_v = 0.76$ along the $v = 0$ and $u = 0$ principal planes, respectively. Figure 6(b) shows the real distribution of the reference excitations, $\{w_{mn}^{ref} = \alpha_{mn}^{ref}; m = 1, \dots, M, n = 1, \dots, N\}$, while the corresponding power pattern, affording a sidelobe level of $SLL = -25$ [dB] and matching the mask $\Psi(u, v)$, is plotted along the principal planes [i.e., $u = 0$ - Fig. 7(b); $v = 0$ - Fig.

7(c)].

By considering the $R = 2$ -th level alphabet of L -tromino rep-tiles with $I^{(R)} \Big|_{R=2} = 12$ elements, the R -order tileability of the aperture A has been successfully checked against the theorem in Sect. 3.1. Indeed, the second condition of the L -tromino covering theorem holds true since $l^{(R)} = 2$. The *RTAM* has been then executed by setting the maximum partitioning of the array to $Q_{max} = 14$ tiles. At the *Step 1* ($h = 0$), $T^{(R)} = 18$ (Tab. I - $\widehat{M} = 4$, $\widehat{N} = 6$) different tilings of the aperture with $I^{(R)}$ -sized L -trominoes have been generated with the Algorithm-X [43][44] and the optimal R -th order tiling, \hat{c}_{opt} , which minimizes the mask matching (8), is shown in Fig. 8(a) where the color level representation of the sub-array excitations, \widehat{w}_{opt} (i.e., $\widehat{w}_{opt} = \{\widehat{w}_q^{opt} = \widehat{\alpha}_q^{opt} e^{j\widehat{\beta}_q^{opt}}; q = 1, \dots, \widehat{Q}\}$), is given, as well. Afterwards ($h = 1$), the *STM* is computed (9) for each q -th ($q = 1, \dots, \widehat{Q}$; $\widehat{Q} = 8$) tile of \hat{c}_{opt} , $\xi_q^{(1)} \Big|_{h=1}$ [Fig. 8(b)], and the tile with the maximum value (i.e., $\widehat{q} = 7$) has been selected (10) and divided into $S = 4$ rep-tiles of level $(R - 1)$ with $I^{(R-1)} = 3$ elements to yield the new array tiling $\mathbf{c}^{(h)} \Big|_{h=1}$ in Fig. 8(c) ($Q^{(h)} \Big|_{h=1} = 11$). Once the $Q^{(1)}$ tiles of $\mathbf{c}^{(1)}$ [Fig. 8(d)] have been ranked (10) according to their *STM* values ($\widehat{q} = 2$) [Fig. 8(d)], a further iteration ($h = 2$) of the *RTAM* has been completed by deriving the tiled arrangement, $\mathbf{c}^{(h)} \Big|_{h=2}$, in Fig. 8(e) ($Q^{(h)} \Big|_{h=2} = 14$ being $Q_r^{(h)} \Big|_{r=R}^{h=2} = 6$ and $Q_r^{(h)} \Big|_{r=R-1}^{h=2} = 8$). The iterative procedure has been stopped (*Step 2.5*) after $H = 2$ iterations since the convergence condition on the maximum number of sub-arrays has been reached (i.e., $Q^{(h)} = Q_{max}$) and the final clustered architecture has been set to the current one ($\mathbf{c}_{opt} = \mathbf{c}^{(2)}$). This latter affords a power pattern [Figs. 7(b)-7(c)] with a mask matching index equal to $\Gamma_{opt} = 7.31 \times 10^{-4}$ [$\Gamma_{opt} \triangleq \Gamma(\mathbf{c}_{opt})$].

To assess the effectiveness and the reliability of the *RTAM* to find the optimal tiling of the aperture A , that is (in other words), to prove that the solution \mathbf{c}_{opt} is the global optimum subject to the constraint $Q \leq Q_{max}$, the Algorithm-X has been used [43][44] in an exhaustive way to generate all clustered layouts with $I^{(R-1)}$ - and $I^{(R)}$ -sized ($R = 2$) L -tromino tiles, each having $B = 4$ possible rotations. Once the whole set of $T \simeq 5.92 \times 10^7$ tilings has been generated, the mask matching index (7) of the $T_{Q_{max}} = 6248$ partitions with $Q \leq Q_{max}$ tiles (i.e., $Q_R = 6$ and $Q_{R-1} = 8$ being $Q = \sum_{r=1}^R Q_r$) has been computed to determine the optimal solution of the problem at hand, $\tilde{\mathbf{c}}_{opt}$. The mask matching value of the $T_{Q_{max}}$ solutions, sorted from

the worst to the best, are reported in Fig. 7(a) and compared to that from the *RTAM* at the convergence, Γ_{opt} . As it can be also inferred by the plots of the power patterns in Figs. 7(b)-7(c), the optimal solution found by the Algorithm-X exhaustive search coincides with the *RTAM* one (i.e., $\mathbf{c}_{opt} \equiv \tilde{\mathbf{c}}_{opt}$), although this latter has been yielded saving the 98.75% of the *CPU* costs (i.e., $\Delta t_{RTAM} < 1$ [min] vs. $\Delta t_X \approx 80$ [min]) on a 1.6GHz PC with 8GB of RAM.

The second example is aimed at pointing out the advantages of using the *L*-tromino rep-tiles instead of the square ones. Indeed, the square geometry belongs to the rep-tiles family since it can be represented as the union of its $S = 4$ smaller copies with halved edge length. Such a comparison has been performed on a benchmark array of $M \times N = 24 \times 24$ isotropic elements spaced by $d_x = d_y = \frac{\lambda}{2}$, while the reference excitations [Fig. 9(b)] have been still synthesized with the *CP* subject to the pattern constraints [i.e., $SLL_1 = -25$ [dB], $SLL_2 = -30$ [dB], $BW_u = BW_v = 0.274$, and $(u_0, v_0 = 0, 0)$] coded by the mask $\Psi(u, v)$ in Fig. 9(a). Moreover, the maximum tiles order has been set to $R = 3$ so that *L*-trominoes with $I_L^{(R-2)} = 3$, $I_L^{(R-1)} = 12$, and $I_L^{(R)} = 48$ elements and squares with $I_S^{(R-2)} = 4$, $I_S^{(R-1)} = 16$, and $I_S^{(R)} = 64$ elements have been used for tiling the array aperture A . Furthermore, Q_{max} has been set to $Q_{max} = 120$ to have a *TRM* reduction of about $\Delta_{TRM}^{min} \approx 79\%$ ($\Delta_{TRM}^{min} = \Delta_{TRM}^Q \Big|_{Q=Q_{max}}$ being $\Delta_{TRM}^Q \triangleq 1 - \frac{Q}{M \times N}$).

Inasmuch as the R -order tileability condition holds true, the *RTAM* has been applied with both *L*-shaped and square tiles. Figure 10 shows the behavior of the mask matching versus the number of sub-arrays, Q , of the H ($H = 36$) layouts generated during the *RTAM* loop. One can notice that the *L*-shaped arrangement always outperforms the corresponding (i.e., $Q_L = Q_S$) square one, more and more as the heavier the clustering ratio is (i.e., $\Delta_{TRM}^Q \rightarrow 100\%$). Table II summarizes the results of the comparative study by reporting the mask matching index along with the key pattern descriptors (i.e., the *SLL*, the directivity, D , and the half-power beamwidth along the azimuth, $HPBW_{az}$, and the elevation, $HPBW_{el}$, planes) for the set of selected layouts with $Q = \{39, 81, 120\}$ rep-tiles. For illustrative purposes, the tilings synthesized at the $h = 23$ -th iteration the *RTAM* with $Q^{(h)} = 81$ tiles are shown in Figs. 11(a)-11(b), while the corresponding power patterns along the $v = 0$ and the $u = 0$ cuts are plotted in Fig. 11(c) and Fig. 11(d), respectively.

The third experiment refers to a wider rectangular aperture A of $M \times N = 24 \times 36$ elements. Because of the array size, the use of an exhaustive tiling approach becomes almost computationally unfeasible. Otherwise, the *RTAM* has been efficiently applied starting from the *CP*-synthesized reference array in Fig. 12(c), which affords the power pattern of Fig. 12(b) that fulfils the pattern mask $\Psi(u, v)$ featuring the following descriptors: $SLL_1 = -25$ [dB], $SLL_2 = -30$ [dB], $BW_u = 0.164$, and $BW_v = 0.274$ [Fig. 12(a)]. More in detail, the *RTAM* has been executed with a rep-tiles alphabet of order $R = 3$ ($I^{(R)} = 48$, $l^{(R)} = 4$, $\widehat{M} = 6$, and $\widehat{N} = 9$) so that the second condition of the covering theorem is fulfilled, while the choice of rep-tiles of higher order (e.g., $R = 4 \rightarrow I^{(R)} = 192$, $l^{(R)} = 8$, $\widehat{M} = 3$, and $\widehat{N} = 5$) would not have guaranteed the complete tileability of A . Moreover, the minimum *TRM* saving has been fixed to $\Delta_{TRM}^{min} \approx 69$ % (i.e., $Q_{max} = 270$).

The *RTAM* has been initialized (*Step 1*) with the $T^{(R)} = 4312$ (i.e., $\widehat{M} = 6$, $\widehat{N} = 9$ - Tab. I) uniform tilings of $\widehat{Q} = 18$ $I^{(R)}$ -sized L -tromino rep-tiles generated by the Algorithm-X. The one, $\widehat{\mathbf{c}}_{opt}$, with minimum mismatch (i.e., $\widehat{\Gamma}_{opt} = \Gamma^{(h)} \Big|_{h=0} = 7.33 \times 10^{-5}$ being $\widehat{\Gamma}_{opt} \triangleq \Gamma(\widehat{\mathbf{c}}_{opt})$ - Tab. III) is shown in Fig. 14(a), the corresponding power pattern being in Fig. 14(e). In the *Step 2*, the *RTAM* loop has been runned for $H = 84$ iterations by generating at each h -th ($h = 1, \dots, H$) iteration a different Q -tiled arrangement (Fig. 13) until the convergence solution with $Q^{(H)} \Big|_{H=84} = 270$ clusters.

Figure 14 includes the layouts [Figs. 14(b)-14(d)] and the corresponding power patterns [Figs. 14(f)-14(h)] for three representative solutions featuring different trade-offs between the number of clusters [i.e., $Q = 48$ - Fig. 14(b) and Fig. 14(f); $Q = 150$ - Fig. 14(c) and Fig. 14(g), and $Q = 270$ - Fig. 14(d) and Fig. 14(h)] and the pattern mask fitting (Fig. 13). More in detail, the solution with $Q = 150$ sub-arrays allows one to reduce of about $\Delta_{TRM}^Q \approx 82.6$ % the number of the *TRMs* of the reference fully-populated layout by radiating a power pattern that deviates of $\Gamma = 5.63 \times 10^{-5}$ from the mask, the *SLL* being only 0.22 [dB] above the reference value ($SLL \Big|_{Q=150} = -24.78$ [dB] vs. $SLL \Big|_{ref} = -25.00$ [dB] - Tab. III). Differently, the tiled configuration with $Q = 48$ clusters further reduces the architectural complexity up to $\Delta_{TRM}^Q \approx 94.4$ %, but it gets worse in terms of mask matching ($\Gamma = 7.33 \times 10^{-5}$ - Tab. III) and sidelobe level ($SLL \Big|_{Q=48} = -21.33$ - Tab. III). As expected, it turns out that the more the sub-

arrays, the smaller the value of the mask matching index is at the cost of a higher complexity of the feeding network (e.g., $Q = 270$, $\Gamma = 7.17 \times 10^{-6}$, $SLL = -24.70$ [dB] - Tab. III). However, it is worth noting from Fig. 13 that the mask-mismatch variations become almost negligible, from a practical viewpoint, when $Q > 150$, since the SLL improves less than 0.1 [dB] as also confirmed by the comparison of the power patterns along the $v = 0$ and $u = 0$ planes in Fig. 15(a) and Fig. 15(b), respectively.

In order to validate the *RTAM* with arrays having non-zero phase excitations, the next experiment addresses the design of the same size array of the previous test case ($M \times N = 24 \times 36$), but fitting a mask $\Psi(u, v)$ steered towards the direction $(u_0, v_0) = (0.0755, 0.0436)$ (i.e., $(\theta_0, \phi_0) = (5, 30)$ [deg]) having $SLL_1 = -20$ [dB], $SLL_2 = -25$ [dB], $BW_u = 0.125$, and $BW_v = 0.2$ [Fig. 16(a)]. Figure 16(b) shows the reference pattern radiated by the *CP*-optimized amplitude and phase coefficients in Fig. 16(c) and Fig. 16(d), respectively.

The behaviour of the mask matching index versus the number of clusters, Q , of the $H = 84$ tiled arrangements iteratively generated by the *RTAM* is shown in Fig. 17, while the pattern features of the layouts having $Q = \{18, 48, 150, 270\}$ are given in Tab. IV, as well. For comparative purposes and analogously to the previous (non-steered) case, the configuration with $Q = 150$ sub-arrays is analyzed. Figure 18 indicates the aperture tiling within the color maps of the corresponding sub-array amplitude [Fig. 18(a)] and phase [Fig. 18(b)] coefficients. Unlike the clustered layouts synthesized for the broadside-steered arrays [e.g., Figs. 11(a)-11(b) and Fig. 14(c)], where wider tiles are placed at the center of the array, the central part of the aperture is here covered by smaller tiles [Figs. 18(a)-18(b)] to better match the complex reference excitations. As for the radiated power pattern, the plots along the main planes in Figs. 18(c)-(d) show non-negligible violations mainly in the mask region with $SLL_2 = -25$ [dB], while the mask matching is satisfactory near the main beam with a SLL violation of only 0.7 [dB] (Tab. IV).

Next, the reliability of the *RTAM*-optimized tiled array when scanning the beam around the pointing direction has been investigated by setting the sub-array phases, $\{\beta_q; q = 1, \dots, Q\}$, according to (6) starting from the reference values

$$\beta_{mn}^{ref} = -k(x_{mn}u_s + y_{mn}v_s) \quad (12)$$

($m = 1, \dots, M$; $n = 1, \dots, N$), where $u_s \triangleq \sin(\theta_0 + \theta_s) \cos(\phi_0 + \phi_s)$ and $v_s \triangleq \sin(\theta_0 + \theta_s) \sin(\phi_0 + \phi_s)$.

Figure 19 shows the color map of the SLL when scanning the beam around the pointing direction $(\theta_0, \phi_0) = (5, 30)$ [deg] within the cone $0 \leq \phi_s < 360$ [deg] and $\theta_s \leq 30$ [deg]. It turns out that $SLL_{max} \leq -14.5$ [dB] and $SLL_{avg} = -18.27$ [dB] for the beam scan region $\{\theta_s \leq 5$ [deg], 0 [deg] $\leq \phi \leq 360$ [deg]\}, SLL_{max} and SLL_{avg} being maximum and the average SLL , respectively.

A further benchmark is concerned with the asymmetric pattern mask of Fig. 20(a), which is centered at broadside with beamwidths $BW_u = 0.080$ and $BW_v = 0.125$ and it is characterized by three sidelobe regions (i.e., $SLL_1 = -20$ [dB], $SLL_2 = -25$ [dB], and $SLL_3 = -30$ [dB]). Such a mask is fulfilled by the power pattern in Fig. 20(b) radiated by a fully-populated array of $M \times N$ elements with excitations in Figs. 20(c)-20(d).

As a representative example, Figure 21 pictorially describes the compromise/intermediate solution, synthesized after $h = 44$ iterations by the *RTAM*, having $Q^{(h)}|_{h=44} = 150$ sub-arrays. As expected, the rep-tiles layout presents the smaller tiles in the regions of the array aperture where there are the most relevant variations in the spatial distribution of the phase and the amplitude of the reference excitations [Figs. 21(a)-21(b)]. As a result, the corresponding pattern faithfully fits the mask constraint along the $v = 0$ cut [Fig. 21(c)], while there are two sidelobes in the $SLL_3 = -30$ [dB] sidelobe suppression region of the $u = 0$ cut that exceed the target bound of about 2 [dB] [Fig. 21(d)].

The last experiment is aimed at giving some insights on the robustness of the *RTAM*-synthesized layout when dealing with non-ideal radiating elements. Towards this end, a realistic antenna element with embedded pattern $e(u, v) \neq 1$ [Fig. 22(a)] has been chosen for the analysis of the previous $Q = 150$ element *RTAM* tiled array. In particular, such a radiating element is a rectangular slot-fed patch antenna of length 1.029 [mm] and width 1.650 [mm], placed over a substrate with $\varepsilon_r = 2.2$ and $\tan\delta = 9 \times 10^{-4}$, that resonates at the working frequency $f = 78.5$ [GHz]. Its embedded element pattern [Fig. 22(a)] has been computed with the

finite-element full-wave solver *Ansys HFSS* [48] by modeling the radiator within a 5×5 set of identical elements [Fig. 22(b)] to take into account the mutual coupling effects as well as other electromagnetic interactions.

The comparison between the real and the ideal pattern along the principal planes is reported in Figs. 21(c)-21(d). One can observe that there are negligible differences in the lobes regions close to end-fire, while the patterns in the mainlobe are indistinguishable as confirmed by the values of the pattern metrics in Tab. V ($\Gamma_{ideal} = 4.44 \times 10^{-6}$ vs. $\Gamma_{real} = 3.77 \times 10^{-6}$ and $SLL_{ideal} = -19.68$ [dB] vs. $SLL_{real} = -20.72$ [dB]).

5 Conclusions

In this work, the design of highly-modular planar *PAs* has been addressed by exploiting the self-replicating property of rep-tiles. An innovative deterministic method has been proposed to synthesize irregular rep-tiles layouts fitting user-defined power pattern requirements, which are mathematically coded in suitable pattern-masks, by jointly minimizing the number of clusters to fully cover the array aperture.

From the numerical assessment, the following outcomes and conclusions can be drawn:

- the proposed *RTAM* is able of converging towards optimal compromise solutions of the constrained synthesis problem at hand by also enabling a non-negligible saving of the computational cost with respect to state-of-the-art exhaustive approaches;
- since the iterative *RTAM* progressively generates multiple clustered array layouts, which are different trade-offs between the number of clusters Q and the fulfilment of the user-defined pattern requirements, it implicitly provides to the user, besides the optimal-matching arrangement at the convergence, a Pareto front of compromise solutions;
- thanks to the deterministic recursive subdivision of wider rep-tiles into smaller ones in correspondence with larger variations of the amplitude/phase distribution of the reference excitations, the *RTAM* is an effective and reliable tool for the design of arbitrary-large/dense arrays;

- L -tromino rep-tiles turn out to be more effective than the square ones since they allow one to better fit the user-defined power pattern mask with less sub-arrays.

Future research activities, beyond the scope of this work, will include the investigation of different rep-tile families and aperture geometries among those of interest for modern PA applications.

Acknowledgements

This work benefited from the networking activities carried out within the Project CYBER-PHYSICAL ELECTROMAGNETIC VISION: Context-Aware Electromagnetic Sensing and Smart Reaction (EMvisioning) (Grant no. 2017HZJXSZ) funded by the Italian Ministry of Education, University, and Research under the PRIN2017 Program (CUP: E64I19002530001). Moreover, it benefited from the networking activities carried out within the Project SPEED (Grant No. 61721001) funded by National Science Foundation of China under the Chang-Jiang Visiting Professorship Program, the Project 'Inversion Design Method of Structural Factors of Conformal Load-bearing Antenna Structure based on Desired EM Performance Interval' (Grant no. 2017HZJXSZ) funded by the National Natural Science Foundation of China, and the Project 'Research on Uncertainty Factors and Propagation Mechanism of Conformal Load-bearing Antenna Structure' (Grant No. 2021JZD-003) funded by the Department of Science and Technology of Shaanxi Province within the Program Natural Science Basic Research Plan in Shaanxi Province. A. Massa wishes to thank E. Vico for her never-ending inspiration, support, guidance, and help.

Appendix

The matrix $\mathbf{G}_{\widehat{M}}$ ($\widehat{M} \geq 1$) is recursively computed as follows

$$\mathbf{G}_{\widehat{M}} = \begin{bmatrix} \mathbf{S}_{\widehat{M}-1} & \mathbf{H}_{\widehat{M}-1} \\ \mathbf{G}_{\widehat{M}-1} & \mathbf{S}_{\widehat{M}-1} \end{bmatrix} \quad (13)$$

where

$$\mathbf{S}_{\widehat{M}} = \begin{bmatrix} \mathbf{Z}_{\widehat{M}-1} & \mathbf{G}_{\widehat{M}-1} \\ \mathbf{Z}_{\widehat{M}-1} & \mathbf{Z}_{\widehat{M}-1} \end{bmatrix} \quad (14)$$

and

$$\mathbf{H}_{\widehat{M}} = \begin{bmatrix} \mathbf{G}_{\widehat{M}-1} & 2 \times \mathbf{S}_{\widehat{M}-1} \\ \mathbf{Z}_{\widehat{M}-1} & \mathbf{G}_{\widehat{M}-1} \end{bmatrix}, \quad (15)$$

$\mathbf{Z}_{\widehat{M}}$ being the $2^{\widehat{M}} \times 2^{\widehat{M}}$ null matrix and setting $\mathbf{G}_{\widehat{M}}|_{\widehat{M}=0} = 1$, $\mathbf{S}_{\widehat{M}}|_{\widehat{M}=0} = 0$, and $\mathbf{H}_{\widehat{M}}|_{\widehat{M}=0} = 0$.

References

- [1] W. Hong, Z. H. Jiang, C. Yu, D. Hou, H. Wang, C. Guo, Y. Hu, L. Kuai, Y. Yu, Z. Jiang, Z. Chen, J. Chen, Z. Yu, J. Zhai, N. Zhang, L. Tian, F. Wu, G. Yang, Z.-C. Hao, and J. Y. Zhou, "The role of millimeter-wave technologies in 5G/6G wireless communications," *IEEE J. Microw.*, vol. 1, no. 1, pp. 101-122, Jan. 2021.
- [2] G. Oliveri, G. Gottardi, and A. Massa, "A new meta-paradigm for the synthesis of antenna arrays for future wireless communications," *IEEE Trans. Antennas Propag.*, vol. 67, no. 6, pp. 3774-3788, Jun. 2019.
- [3] Y. Yu, Z. H. Jiang, H. Zhang, Z. Zhang, and W. Hong, "A low-profile beamforming patch array with a cosecant fourth power pattern for millimeter-wave synthetic aperture radar applications," *IEEE Trans. Antennas Propag.*, vol. 68, no. 9, pp. 6486-6496, Sep. 2020.
- [4] C. Waldschmidt, J. Hasch, and W. Menzel, "Automotive radar - From first efforts to future systems," *IEEE J. Microw.*, vol. 1, no. 1, pp. 135-148, Jan. 2021.
- [5] J.-J. Peng, S.-W. Qu, M. Xia, and S. Yang, "Conformal phased array antenna for unmanned aerial vehicle with +/-70 [deg] scanning range," *IEEE Trans. Antennas Propag.*, vol. 69, no. 8, pp. 4580-4587, Aug. 2021.
- [6] Y. Yang, Z. Fan, T. Hong, M. Chen, X. Tang, J. He, X. Chen, C. Liu, H. Zhu, and K. Huang, "Design of microwave directional heating system based on phased-array antenna," *IEEE Trans. Microw. Theory Tech.*, vol. 68, no. 11, pp. 4896-4904, Nov. 2020.

- [7] S. Li, S. Wang, Q. An, G. Zhao, and H. Sun, "Cylindrical MIMO array-based near-field microwave imaging," *IEEE Trans. Antennas Propag.*, vol. 69, no. 1, pp. 612-617, Jan. 2021.
- [8] X. Gu, A. Valdes-Garcia, A. Natarajan, B. Sadhu, D. Liu, and S. K. Reynolds, "W-band scalable phased arrays for imaging and communications," *IEEE Comm. Mag.*, vol. 53, no. 4, pp. 196-204, Apr. 2015.
- [9] J. S. Herd and M. D. Conway, "The evolution to modern phased array architectures," *Proc. IEEE*, vol. 104, no. 3, pp. 519-529, Mar. 2016.
- [10] A. S. Abdellatif, W. Zhai, H. K. Pothula, and M. Repeta, "Array of arrays: optimizing phased array tiles," *IEEE Antennas Wireless Propag. Lett.*, vol. 20, no. 5, pp. 718-722, May 2021.
- [11] P. Rocca, G. Oliveri, R. J. Mailloux, and A. Massa, "Unconventional phased array architectures and design methodologies - A review," *Proc. IEEE*, vol. 104, no. 3, pp. 544-560, Mar. 2016.
- [12] G. Oliveri, G. Gottardi, M. A. Hannan, N. Anselmi, and L. Poli, "Autocorrelation-driven synthesis of antenna arrays - The case of DS-based planar isophoric thinned arrays," *IEEE Trans. Antennas Propag.*, vol. 68, no. 4, pp. 2895-2910, Apr. 2020.
- [13] L. Poli, P. Rocca, M. Salucci, and A. Massa, "Reconfigurable thinning for the adaptive control of linear arrays," *IEEE Trans. Antennas Propag.*, vol. 61, no. 10, pp. 5068-5077, Oct. 2013.
- [14] M. Carlin, G. Oliveri, and A. Massa, "Hybrid BCS-deterministic approach for sparse concentric ring isophoric arrays," *IEEE Trans. Antennas Propag.*, vol. 63, no. 1, pp. 378-383, Jan. 2015.
- [15] N. Viswanathan, S. Venkatesh, and D. Schurig, "Optimization of a sparse aperture configuration for millimeter-wave computational imaging," *IEEE Trans. Antennas Propag.*, vol. 69, no. 2, pp. 1107-1117, Feb. 2021.

- [16] L. Manica, P. Rocca, A. Martini, and A. Massa, "An innovative approach based on a tree-searching algorithm for the optimal matching of independently optimum sum and difference excitations," *IEEE Trans. Antennas Propag.*, vol. 56, no. 1, pp. 58-66, Jan. 2008.
- [17] P. Rocca, M. H. Hannan, L. Poli, N. Anselmi, and A. Massa, "Optimal phase-matching strategy for beam scanning of sub-arrayed phased arrays," *IEEE Trans. Antennas and Propag.*, vol. 67, no. 2, pp. 951-959, Feb. 2019.
- [18] N. Anselmi, P. Rocca, M. Salucci, and A. Massa, "Contiguous phase-clustering in multibeam-on-receive scanning arrays," *IEEE Trans. Antennas Propag.*, vol. 66, no. 11, pp. 5879-5891, Nov. 2018.
- [19] N. Anselmi, G. Gottardi, G. Oliveri, and A. Massa, "A total-variation sparseness-promoting method for the synthesis of contiguously clustered linear architectures" *IEEE Trans. Antennas Propag.*, vol. 67, no. 7, pp. 4589-4601, Jul. 2019.
- [20] X. Yang, W. Xi, Y. Sun, T. Zeng, T. Long, and T. K. Sarkar, "Optimization of subarray partition for large planar phased array radar based on weighted K-means clustering method," *IEEE J. Sel. Topics Signal Process.*, vol. 9, no. 8, pp. 1460-1468, Dec. 2015.
- [21] P. Rocca, M. D'Urso, and L. Poli, "Advanced sub-arraying strategy for large antenna array design with sub-array-only control," *IEEE Antennas Wireless Propag. Lett.*, vol. 13, pp. 91-94, 2014.
- [22] P. Rocca, R. J. Mailloux, and G. Toso, "GA-based optimization of irregular sub-array layouts for wideband phased arrays design," *IEEE Antennas Wireless Propag. Lett.*, vol. 14, pp. 131-134, 2015.
- [23] M. D'Urso, M. G. Labate, A. Buonanno, and P. Vinetti, "Effective beam forming networks for large arbitrary array of antennas," *IEEE Trans. Antennas Propag.*, vol. 60, no. 11, pp. 5129-5135, Nov. 2012.

- [24] Z-Y. Xiong, Z-H. Xu, S-W. Chen, and S-P. Xiao, "Subarray partition in array antenna based on the algorithm X," *IEEE Antennas Wireless Propag. Lett.*, vol. 12, pp. 906-909, 2013.
- [25] N. Anselmi, P. Rocca, M. Salucci, and A. Massa, "Irregular phased array tiling by means of analytic schemata-driven optimization," *IEEE Trans. Antennas Propag.*, vol. 65, no. 9, pp. 4495-4510, Sep. 2017.
- [26] R. Zhang, H. Zhang, W. Xu, and X. You, "Subarray-based simultaneous beam training for multiuser mmwave massive MIMO systems," *IEEE Wireless Commun. Lett.*, vol. 8, no. 4, pp. 976-979, Aug. 2019.
- [27] Y. Ma, S. Yang, Y. Chen, S. Qu, and J. Hu, "Pattern synthesis of 4-D irregular antenna arrays based on maximum-entropy model," *IEEE Trans. Antennas Propag.*, vol. 67, no. 5, pp. 3048-3057, May 2019.
- [28] P. Rocca, N. Anselmi, A. Polo, and A. Massa, "Modular design of hexagonal phased arrays through diamond tiles," *IEEE Trans. Antennas Propag.*, vol. 68, no. 5, pp. 3598-3612, May 2020.
- [29] E. Bekker, J. W. Odendaal, and J. Joubert, "Optimized polarization for rotationally tiled, wideband, dual-polarized Vivaldi arrays," *Proc. 14th European Conf. Antennas Propag. (EuCAP)*, Copenhagen, Denmark, 15-20 Mar. 2020.
- [30] W. Dong, Z. Xu, X. Liu, L. Wang, and S. Xiao, "Irregular subarray tiling via heuristic iterative convex relaxation programming," *IEEE Trans. Antennas Propag.*, vol. 68, no. 4, pp. 2842-2852, Apr. 2020.
- [31] G. Oliveri, M. Salucci, and A. Massa, "Synthesis of modular contiguously clustered linear arrays through a sparseness-regularized solver," *IEEE Trans. Antennas Propag.*, vol. 64, no. 10, pp. 4277-4287, Oct. 2016.
- [32] G. Oliveri, G. Gottardi, F. Robol, A. Polo, L. Poli, M. Salucci, M. Chuan, C. Massagrande, P. Vinetti, M. Mattivi, R. Lombardi, and A. Massa, "Codesign of unconventional array

- architectures and antenna elements for 5G base stations,” *IEEE Trans. Antennas Propag.*, vol. 65, no. 12, pp. 6752-6767, Dec. 2017.
- [33] D. J. Bekers, S. Jacobs, S. Monni, R. J. Bolt, D. Fortini, P. Capece, and G. Toso, “A Ka-band spaceborne synthetic aperture radar instrument: a modular sparse array antenna design,” *IEEE Antennas Propag. Mag.*, vol. 61, no. 5, pp. 97-104, Oct. 2019.
- [34] P. Rocca, N. Anselmi, A. Polo, and A. Massa, “An irregular two-sizes square tiling method for the design of isophoric phased arrays,” *IEEE Trans. Antennas Propag.*, vol. 68, no. 6, pp. 4437-4449, Jun. 2020.
- [35] B. Rupakula, A. H. Aljuhani, and G. M. Rebeiz, “Limited scan-angle phased-arrays using randomly-grouped subarrays and reduced number of phase-shifters,” *IEEE Trans. Antennas Propag.*, vol. 68, no. 1, Jan. 2020.
- [36] R. J. Mailloux, S. G. Santarelli, T. M. Roberts, and D. Luu, “Irregular polyomino-shaped subarrays for space-based active arrays,” *Int. J. Antennas Propag.*, vol. 2009, no. 956524, pp. 1-9, 2009.
- [37] R. J. Mailloux, *Phased Array Antenna Handbook*, 2nd ed. Norwood, MA: Artech House, 2005.
- [38] S. W. Golomb, “Replicating figures in the plane,” *Math. Gaz.*, vol. 48, no. 366, pp. 403-412, Dec. 1964.
- [39] M. Gardner, “Rep-Tiles,” *The Colossal Book of Mathematics: Classic Puzzles, Paradoxes, and Problems*, W. W. Norton, pp. 46-58, 2001.
- [40] E. A. Robinson, “On the table and the chair,” *Indag. Mathem.*, vol. 10, no. 4, pp. 581-599, Dec. 1999.
- [41] A. Julien and J. Savinien, “K-theory of the chair tiling via AF-algebras.” *J. Geom. Phys.*, vol. 106, pp. 314-326, May 2016.
- [42] R. Fathauer, “Matching rules, aperiodic Tiles, and substitution tilings,” *Tessellations: Mathematics, Art, and Recreation*, CRC Press, NY, 2021.

- [43] D. E. Knuth, "Dancing links," *Millenial Perspectives in Computer Science*, pp. 187-214, 2000.
- [44] N. Anselmi, P. Rocca, S. Feuchtinger, B. Biscontini, A. Murillo-Barrera, and A. Massa, "Optimal capacity-driven design of aperiodic clustered phased arrays for multi-user MIMO communication systems," *IEEE Trans. Antennas Propag.*, vol. 70, no. 7, pp. 5491-5505, Jul. 2022.
- [45] I. Chu and R. Johnsonbaugh, "Tiling boards with trominoes," *J. Recreat. Math.*, vol. 18, no. 3, pp. 188-193, 1958.
- [46] C. Ueno, "Matrices and tilings with right trominoes, " *Math. Mag.*, vol. 81, no. 5, pp. 319-331, 2008.
- [47] T. Isernia, F. A. Pena, O. M. Bucci, M. D'Urso, J. F. Gomez, and J. A. Rodriguez, "A hybrid approach for the optimal synthesis of pencil beams through array antennas," *IEEE Trans. Antennas Propag.*, vol. 52, no. 11, pp. 2912-2918, Nov. 2004.
- [48] ANSYS Electromagnetics Suite-HFSS, ANSYS, Canonsburg, PA, USA, 2019.

FIGURE CAPTIONS

- **Figure 1.** Sketch of a tiled architecture.
- **Figure 2.** *Illustrative Example* ($R = 3, B = 4, S = 4, I^{(r)} \Big|_{r=1} = 3$ - L -tromino rep-tiles) - Sketch of (a) the alphabet Σ and (b) the composition rule.
- **Figure 3.** *Illustrative Example* ($M = 3, N = 4, B = 4, I^{(r)} \Big|_{r=1} = 3$ - L -tromino rep-tiles) - Sketch of the tiling vector $\mathbf{c} = \{1, 1, 2, 2, 1, 3, 4, 2, 3, 3, 4, 4\}$.
- **Figure 4.** *Illustrative Example* ($R = 3, B = 4, I^{(r)} \Big|_{r=1} = 3 \rightarrow I^{(R)} = 48 \rightarrow l^{(R)} = 4$ - L -tromino rep-tiles) - Sketch of (a)(c)(e) tileable and (b)(d)(f) non-tileable apertures: (a) $M = 12$ and $N = 16 \rightarrow \widehat{M} = 3$ ($\widehat{M} \triangleq \frac{M}{l^{(R)}}$) and $\widehat{N} = 4$ ($\widehat{N} \triangleq \frac{N}{l^{(R)}}$) is even, (b) $M = 12$ and $N = 20 \rightarrow \widehat{M} = 3$ but $\widehat{N} = 5$ is odd, (c) $M = 24$ and $N = 8 \rightarrow \widehat{M} \neq 3$ and $\lfloor \frac{M \times N}{l^{(R)}} \rfloor = 0$, (d) $M = 20$ and $N = 8 \rightarrow \widehat{M} \neq 3$ but $\lfloor \frac{M \times N}{l^{(R)}} \rfloor = 16$, (e) $M = 36$ and $N = 24 \rightarrow \widehat{M} \neq 3$ and $\lfloor \frac{M \times N}{l^{(R)}} \rfloor = 0$, and (f) $M = 32$ and $N = 28 \rightarrow \widehat{M} \neq 3$ but $\lfloor \frac{M \times N}{l^{(R)}} \rfloor = 32$.
- **Figure 5.** *Illustrative Example* ($M = 12, N = 16, R = 3, B = 4, S = 4, I^{(r)} \Big|_{r=1} = 3, H = 3$ - L -tromino rep-tiles) - Sketch of (a)(c)(e) rep-tiled array layout and (b)(d)(f) rep-tile splitting at the *RTAM* iteration (a) $h = 0$, (b)(c) $h = 1$, (d)(e) $h = 2$, and (f) $h = H$.
- **Figure 6.** *Numerical Validation* ($M = 8, N = 12, \mathbf{e}(u, v) = 1, d_x = d_y = \frac{\lambda}{2}, (u_0, v_0) = (0, 0) \rightarrow (\theta_0, \phi_0) = (0, 0)$ [deg]) - Color maps of (a) the power pattern mask $\Psi(u, v)$ and (b) the amplitude distribution of the reference excitations, $\{w_{mn}^{ref} = \alpha_{mn}^{ref}; m = 1, \dots, M, n = 1, \dots, N\}$.
- **Figure 7.** *Numerical Validation* ($M = 8, N = 12, \mathbf{e}(u, v) = 1, d_x = d_y = \frac{\lambda}{2}, (u_0, v_0) = (0, 0) \rightarrow (\theta_0, \phi_0) = (0, 0)$ [deg]; $Q_{max} = 14, R = 2, I^{(R)} = 12, I^{(R-1)} = 3$) - Plots of (a) the ranked values of the mask matching index of the $T_{Q_{max}} = 6248$ aperture partitions with $Q \leq Q_{max}$ tiles from the Algorithm-X together with the one, Γ_{opt} , of the *RTAM* optimal solution, \mathbf{c}_{opt} , and (b)(c) the normalized power patterns along the (b) $v = 0$ (i.e., $\phi = 0$ [deg]) and (c) $u = 0$ (i.e., $\phi = 90$ [deg]) planes.

- **Figure 8.** *Numerical Validation* ($M = 8, N = 12, \mathbf{e}(u, v) = 1, d_x = d_y = \frac{\lambda}{2}, (u_0, v_0) = (0, 0) \rightarrow (\theta_0, \phi_0) = (0, 0)$ [deg]; $Q_{max} = 14, R = 2, I^{(R)} = 12, I^{(R-1)} = 3$) - Color maps of (a)(c)(e) amplitude distribution of the clustered excitations, $\{w_q^{(h)} = \alpha_q^{(h)} e^{j\beta_q^{(h)}}; q = 1, \dots, Q^{(h)}\}$, and (b)(d) STM value within the array aperture at the RTAM iterations (a)(b) $h = 0$ ($Q^{(h)} = 8$), (c)(d) $h = 1$ ($Q^{(h)} = 11$), and (e) $h = H$ ($H = 2$) ($Q^{(h)} = Q_{max}$).
- **Figure 9.** *Numerical Validation* ($M = 24, N = 24, \mathbf{e}(u, v) = 1, d_x = d_y = \frac{\lambda}{2}, (u_0, v_0) = (0, 0) \rightarrow (\theta_0, \phi_0) = (0, 0)$ [deg]) - Color maps of (a) the power pattern mask $\Psi(u, v)$ and (b) the amplitude distribution of the reference excitations, $\{w_{mn}^{ref} = \alpha_{mn}^{ref}; m = 1, \dots, M, n = 1, \dots, N\}$.
- **Figure 10.** *Numerical Validation* ($M = 24, N = 24, \mathbf{e}(u, v) = 1, d_x = d_y = \frac{\lambda}{2}, (u_0, v_0) = (0, 0) \rightarrow (\theta_0, \phi_0) = (0, 0)$ [deg]; $Q_{max} = 120, R = 3, I_L^{(R)} = 48, I_L^{(R-1)} = 12, I_L^{(R-2)} = 3, I_S^{(R)} = 64, I_S^{(R-1)} = 16, I_S^{(R-2)} = 4$) - Plot of the mask matching value, $\Gamma^{(h)}$, of the tiled array configuration, $\mathbf{c}^{(h)}$ [i.e., $\Gamma^{(h)} \triangleq \Gamma(\mathbf{c}^{(h)})$], synthesized at the h -th ($h = 0, \dots, H; H = 36$) RTAM loop versus its number of sub-arrays, $Q^{(h)}$.
- **Figure 11.** *Numerical Validation* ($M = 24, N = 24, \mathbf{e}(u, v) = 1, d_x = d_y = \frac{\lambda}{2}, (u_0, v_0) = (0, 0) \rightarrow (\theta_0, \phi_0) = (0, 0)$ [deg]; $Q_{max} = 120, R = 3, I_L^{(R)} = 48, I_L^{(R-1)} = 12, I_L^{(R-2)} = 3, I_S^{(R)} = 64, I_S^{(R-1)} = 16, I_S^{(R-2)} = 4, h = 60, Q^{(h)} \Big|_{h=60} = 81$) - Plots of (a)(b) amplitude distributions of the excitations, $\{w_q^{(h)} = \alpha_q^{(h)} e^{j\beta_q^{(h)}}; q = 1, \dots, Q^{(h)}\}$, of the array tiled with (a) L-trominoes or (b) squares and (c)(d) the normalized power patterns along the (c) $v = 0$ (i.e., $\phi = 0$ [deg]) and (d) $u = 0$ (i.e., $\phi = 90$ [deg]) planes.
- **Figure 12.** *Numerical Validation* ($M = 24, N = 36, \mathbf{e}(u, v) = 1, d_x = d_y = \frac{\lambda}{2}, (u_0, v_0) = (0, 0) \rightarrow (\theta_0, \phi_0) = (0, 0)$ [deg]) - Plots of (a) the power pattern mask $\Psi(u, v)$ and (b) the normalized power pattern radiated by (c) the amplitude distribution of the reference excitations, $\{w_{mn}^{ref} = \alpha_{mn}^{ref}; m = 1, \dots, M, n = 1, \dots, N\}$.
- **Figure 13.** *Numerical Validation* ($M = 24, N = 36, \mathbf{e}(u, v) = 1, d_x = d_y = \frac{\lambda}{2}, (u_0, v_0) = (0, 0) \rightarrow (\theta_0, \phi_0) = (0, 0)$ [deg]; $Q_{max} = 270, R = 3, I^{(R)} = 48, I^{(R-1)} = 12, I^{(R-2)} = 3$) - Plot of the mask matching value, $\Gamma^{(h)}$, of the tiled array configuration, $\mathbf{c}^{(h)}$

[i.e., $\Gamma^{(h)} \triangleq \Gamma(\mathbf{c}^{(h)})$], synthesized at the h -th ($h = 0, \dots, H; H = 84$) *RTAM* loop versus versus its number of sub-arrays, $Q^{(h)}$.

- **Figure 14.** *Numerical Validation* ($M = 24, N = 36, \mathbf{e}(u, v) = 1, d_x = d_y = \frac{\lambda}{2}, (u_0, v_0) = (0, 0) \rightarrow (\theta_0, \phi_0) = (0, 0)$ [deg]; $Q_{max} = 270, R = 3, I^{(R-2)} = 48, I^{(R-1)} = 12, I^{(R)} = 3$) - Plots of (a)(b)(c)(d) the amplitude distribution of the clustered excitations, $\{w_q^{(h)} = \alpha_q^{(h)}; q = 1, \dots, Q^{(h)}\}$, and (e)(f)(g)(h) the corresponding normalized power pattern at the *RTAM* iterations (a)(e) $h = 0$ ($Q^{(h)} = 18$), (b)(f) $h = 10$ ($Q^{(h)} = 48$), (c)(g) $h = 44$ ($Q^{(h)} = 150$), and (d)(h) $h = H$ ($H = 84$) ($Q^{(h)} = Q_{max}$).
- **Figure 15.** *Numerical Validation* ($M = 24, N = 36, \mathbf{e}(u, v) = 1, d_x = d_y = \frac{\lambda}{2}, (u_0, v_0) = (0, 0) \rightarrow (\theta_0, \phi_0) = (0, 0)$ [deg]; $Q_{max} = 270, R = 3, I^{(R)} = 48, I^{(R-1)} = 12, I^{(R-2)} = 3$) - Plots of the normalized power patterns along (a) the $v = 0$ (i.e., $\phi = 0$ [deg]) and (b) the $u = 0$ (i.e., $\phi = 90$ [deg]) planes.
- **Figure 16.** *Numerical Validation* ($M = 24, N = 36, \mathbf{e}(u, v) = 1, d_x = d_y = \frac{\lambda}{2}, (u_0, v_0) = (0.0755, 0.0436) \rightarrow (\theta_0, \phi_0) = (5, 30)$ [deg]; $Q_{max} = 270, R = 3, I^{(R)} = 48, I^{(R-1)} = 12, I^{(R-2)} = 3$) - Plots of (a) the power pattern mask $\Psi(u, v)$ and (b) the normalized power pattern radiated by (c) the amplitude and (d) the phase distributions of the reference excitations, $\{w_{mn}^{ref} = \alpha_{mn}^{ref} e^{j\beta_{mn}^{ref}}; m = 1, \dots, M, n = 1, \dots, N\}$.
- **Figure 17.** *Numerical Validation* ($M = 24, N = 36, \mathbf{e}(u, v) = 1, d_x = d_y = \frac{\lambda}{2}, (u_0, v_0) = (0.0755, 0.0436) \rightarrow (\theta_0, \phi_0) = (5, 30)$ [deg]; $Q_{max} = 270, R = 3, I^{(R-2)} = 48, I^{(R-1)} = 12, I^{(R)} = 3$) - Plot of the mask matching value, $\Gamma^{(h)}$, of the tiled array configuration, $\mathbf{c}^{(h)}$ [i.e., $\Gamma^{(h)} \triangleq \Gamma(\mathbf{c}^{(h)})$], synthesized at the h -th ($h = 0, \dots, H, H = 90$) *RTAM* loop versus its number of sub-arrays, $Q^{(h)}$.
- **Figure 18.** *Numerical Validation* ($M = 24, N = 36, \mathbf{e}(u, v) = 1, d_x = d_y = \frac{\lambda}{2}, (u_0, v_0) = (0.0755, 0.0436) \rightarrow (\theta_0, \phi_0) = (5, 30)$ [deg]; $Q_{max} = 270, R = 3, I^{(R-2)} = 48, I^{(R-1)} = 12, I^{(R)} = 3; h = 44, Q^{(h)} \Big|_{h=44} = 150$) - Plots of (a) the amplitude and (b) the phase distributions of the *RTAM*-synthesized excitations, $\{w_q^{(h)} = \alpha_q^{(h)} e^{j\beta_q^{(h)}}; q = 1, \dots, Q^{(h)}\}$, and (c)(d) the normalized power patterns along the (c) $v = 0$ (i.e., $\phi = 0$ [deg]) and (d) $u = 0$ (i.e., $\phi = 90$ [deg]) planes.

- **Figure 19.** *Numerical Validation* ($M = 24, N = 36, \mathbf{e}(u, v) = 1, d_x = d_y = \frac{\lambda}{2}, (u_0, v_0) = (0.0755, 0.0436) \rightarrow (\theta_0, \phi_0) = (5, 30)$ [deg]; $Q_{max} = 270, R = 3, I^{(R-2)} = 48, I^{(R-1)} = 12, I^{(R)} = 3; h = 44, Q^{(h)} \Big|_{h=44} = 150$) - Color map of the *SLL* variations when scanning the beam around the pointing direction $(\theta_0, \phi_0) = (5, 30)$ [deg] within the cone $0 \leq \phi_s < 360$ [deg] and $\theta_s \leq 30$ [deg].
- **Figure 20.** *Numerical Validation* ($M = 24, N = 36, \mathbf{e}(u, v) = 1, d_x = d_y = \frac{\lambda}{2}, (u_0, v_0) = (0, 0) \rightarrow (\theta_0, \phi_0) = (0, 0)$ [deg]) - Plots of (a) the power pattern mask $\Psi(u, v)$ and (b) the normalized power pattern radiated by (c) the amplitude and (d) the phase distributions of the reference excitations, $\{w_{mn}^{ref} = \alpha_{mn}^{ref} e^{j\beta_{mn}^{ref}}; m = 1, \dots, M, n = 1, \dots, N\}$.
- **Figure 21.** *Numerical Validation* ($M = 24, N = 36, \mathbf{e}(u, v) = 1, d_x = d_y = \frac{\lambda}{2}, (u_0, v_0) = (0, 0) \rightarrow (\theta_0, \phi_0) = (0, 0)$ [deg]; $Q_{max} = 270, R = 3, I^{(R-2)} = 48, I^{(R-1)} = 12, I^{(R)} = 3; h = 44, Q^{(h)} \Big|_{h=44} = 150$) - Plots of (a) the amplitude and (b) the phase distributions of the *RTAM*-synthesized excitations, $\{w_q^{(h)} = \alpha_q^{(h)} e^{j\beta_q^{(h)}}; q = 1, \dots, Q^{(h)}\}$, and (c)(d) the normalized power patterns along the (c) $v = 0$ (i.e., $\phi = 0$ [deg]) and (d) $u = 0$ (i.e., $\phi = 90$ [deg]) planes.
- **Figure 22.** *Numerical Validation* - Plot of the (a) embedded element pattern of the real elementary radiator simulated within (b) a 5×5 set of identical elements.

TABLE CAPTIONS

- **Table I.** *Illustrative Example* - Number of *L*-tromino tilings of *R*-th order (i.e., *T* value).
- **Table II.** *Numerical Validation* ($M = 24, N = 24, \mathbf{e}(u, v) = 1, d_x = d_y = \frac{\lambda}{2}, (u_0, v_0) = (0, 0) \rightarrow (\theta_0, \phi_0) = (0, 0)$ [deg]; $Q_{max} = 120, R = 3, I_L^{(R)} = 48, I_L^{(R-1)} = 12, I_L^{(R-2)} = 3, I_S^{(R)} = 64, I_S^{(R-1)} = 16, I_S^{(R-2)} = 4$) - Pattern features and mask matching index.
- **Table III.** *Numerical Validation* ($M = 24, N = 36, \mathbf{e}(u, v) = 1, d_x = d_y = \frac{\lambda}{2}, (u_0, v_0) = (0.0755, 0.0436) \rightarrow (\theta_0, \phi_0) = (5, 30)$ [deg]; $Q_{max} = 270, R = 3, I^{(R)} = 48, I^{(R-1)} = 12, I^{(R-2)} = 3$) - Pattern features and mask matching index.

- **Table IV.** *Numerical Validation* ($M = 24, N = 36, \mathbf{e}(u, v) = 1, d_x = d_y = \frac{\lambda}{2}, (u_0, v_0) = (0.0755, 0.0436) \rightarrow (\theta_0, \phi_0) = (5, 30)$ [deg]; $Q_{max} = 270, R = 3, I^{(R)} = 48, I^{(R-1)} = 12, I^{(R-2)} = 3$) - Pattern features and mask matching index.
- **Table V.** *Numerical Validation* ($M = 24, N = 36, d_x = d_y = \frac{\lambda}{2}, (u_0, v_0) = (0, 0) \rightarrow (\theta_0, \phi_0) = (0, 0)$ [deg]; ; $Q_{max} = 270, R = 3, I^{(R-2)} = 48, I^{(R-1)} = 12, I^{(R)} = 3$) - Pattern features and mask matching index.

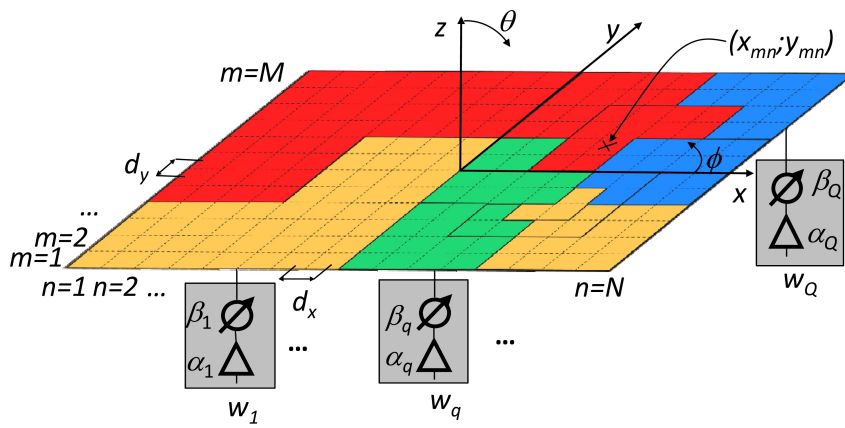
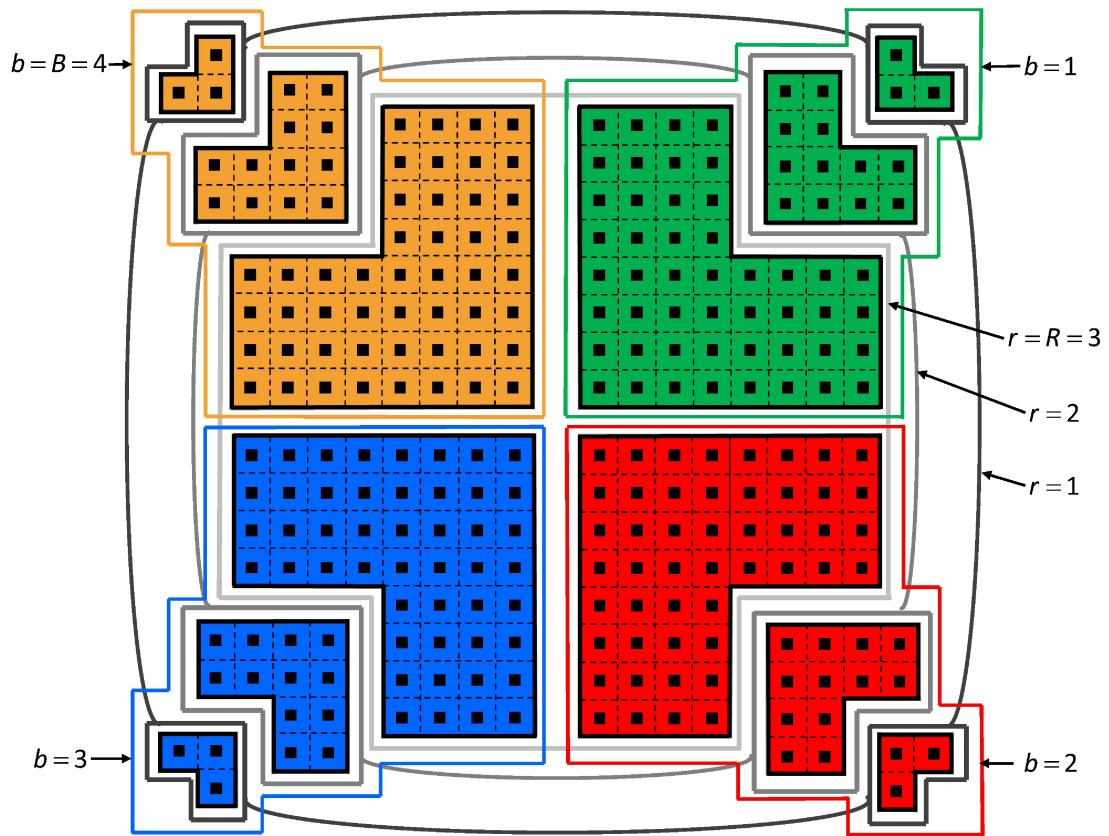
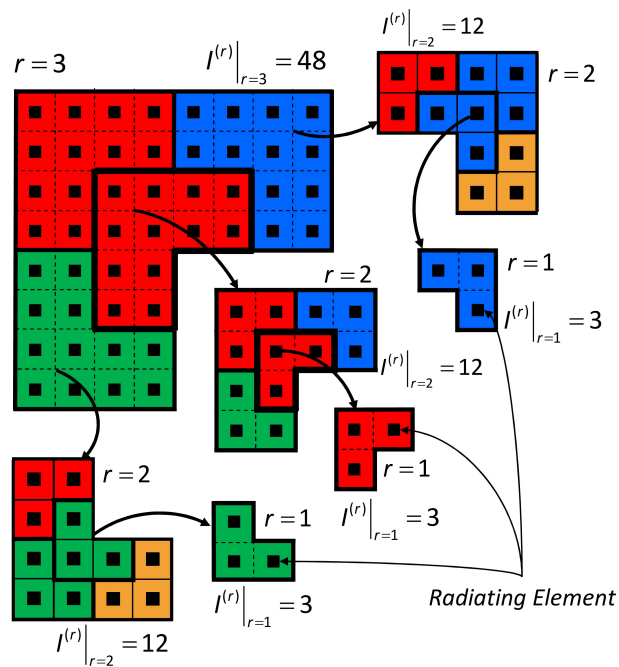


Fig. 1 - N. Anselmi *et al.*, “A Self-Replicating Single-Shape Tiling Technique ...”



(a)



(b)

Fig. 2 - N. Anselmi *et al.*, "A Self-Replicating Single-Shape Tiling Technique ..."

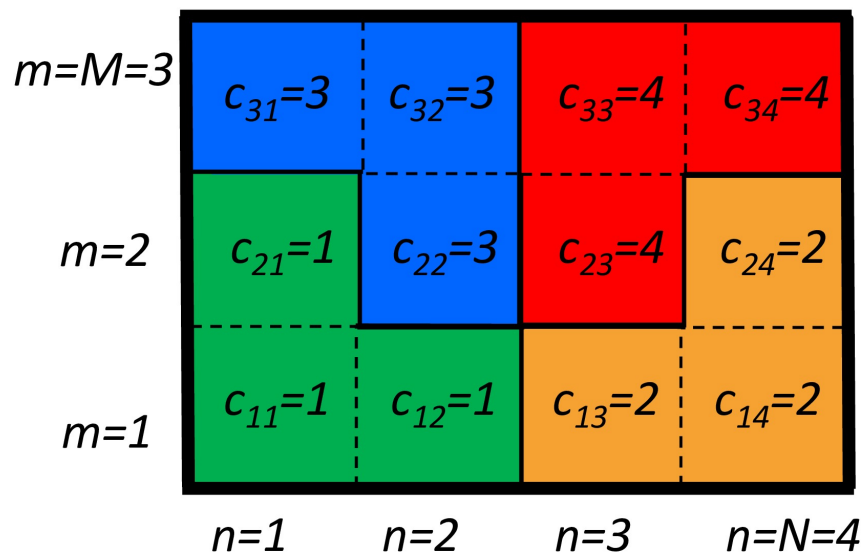


Fig. 3 - N. Anselmi *et al.*, “A Self-Replicating Single-Shape Tiling Technique ...”

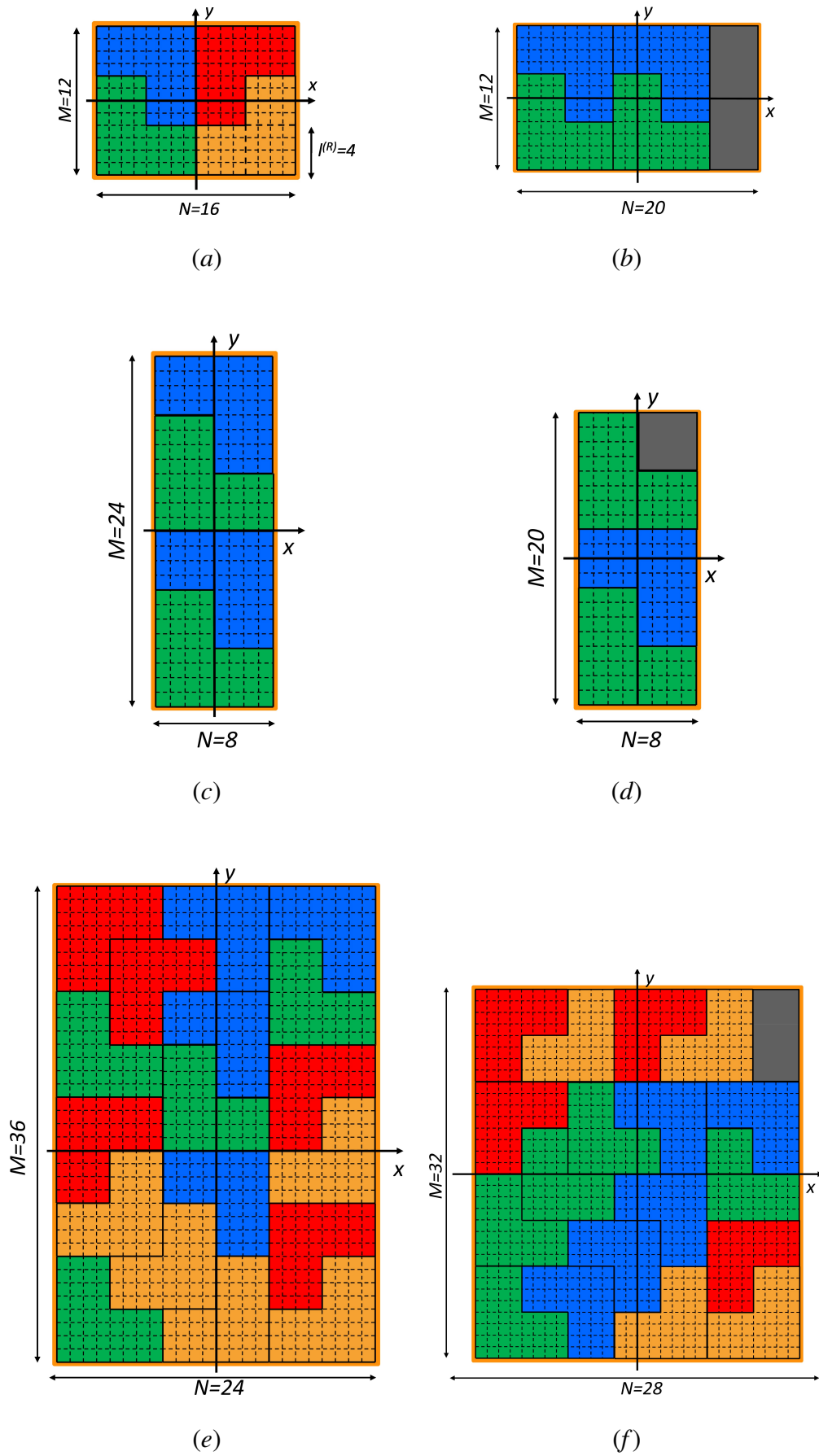


Fig. 4 - N. Anselmi *et al.*, "A Self-Replicating Single-Shape Tiling Technique ..."

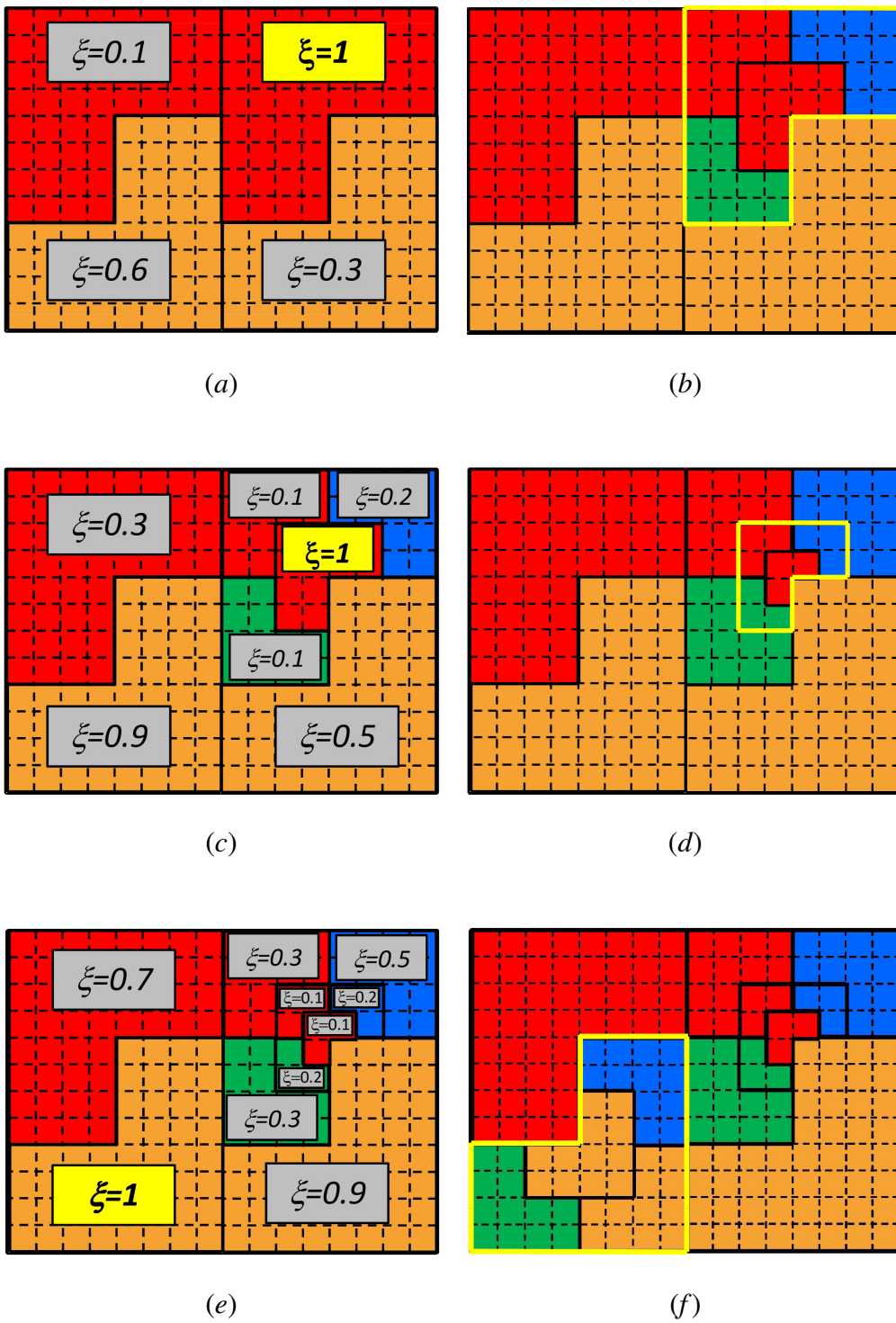
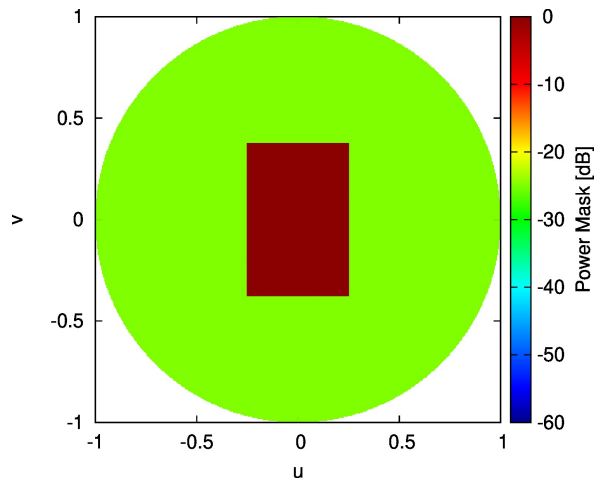
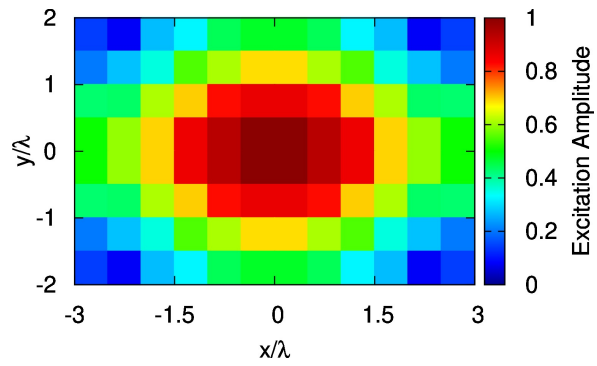


Fig. 5 - N. Anselmi *et al.*, “A Self-Replicating Single-Shape Tiling Technique ...”

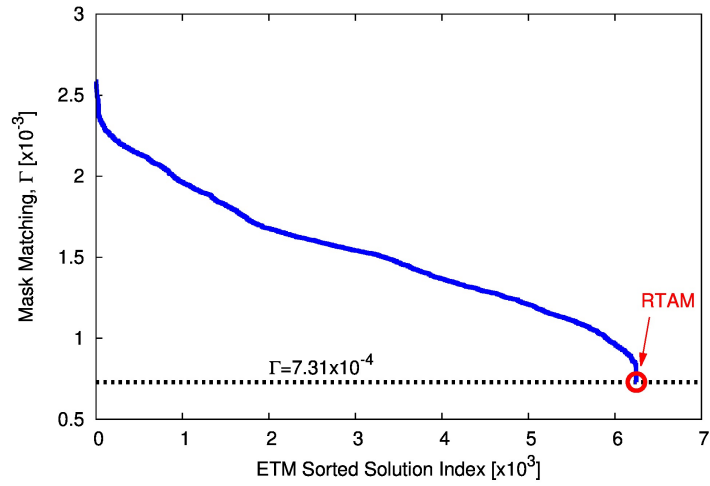


(a)

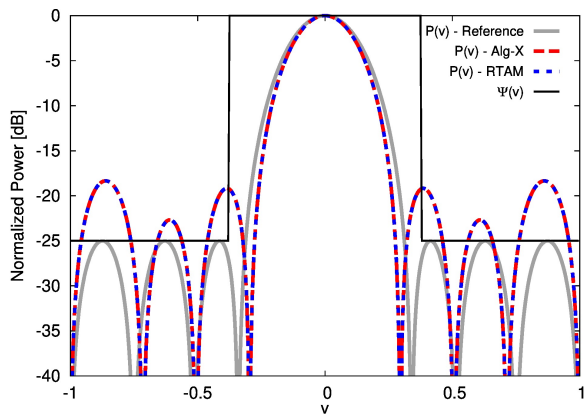


(b)

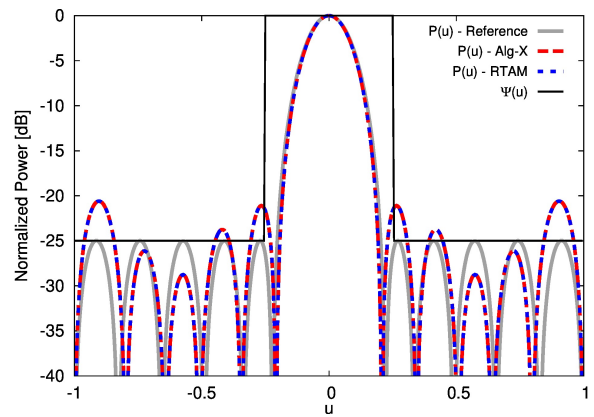
Fig. 6 - N. Anselmi *et al.*, “A Self-Replicating Single-Shape Tiling Technique ...”



(a)



(b)



(c)

Fig. 7 - N. Anselmi *et al.*, “A Self-Replicating Single-Shape Tiling Technique ...”

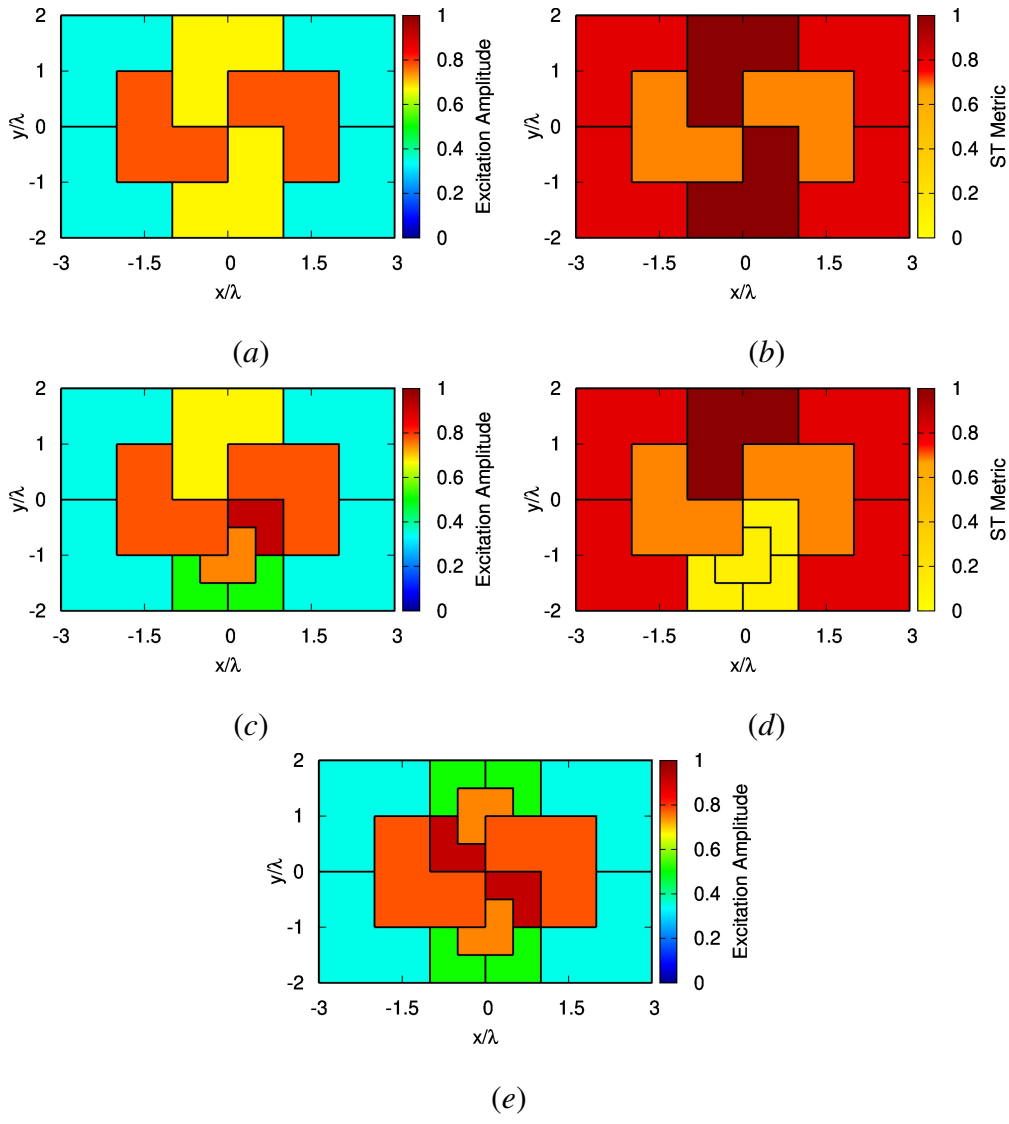
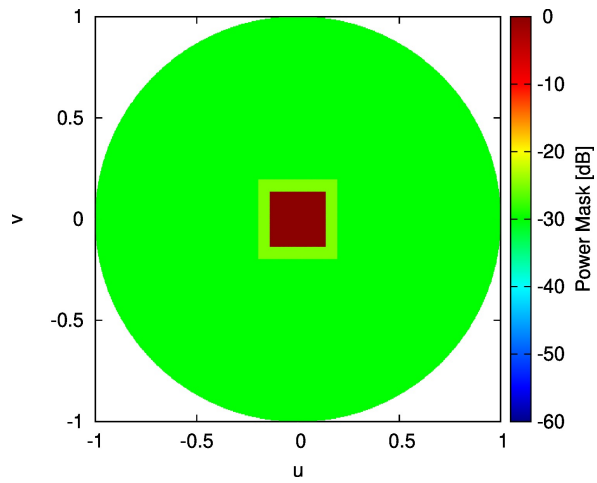
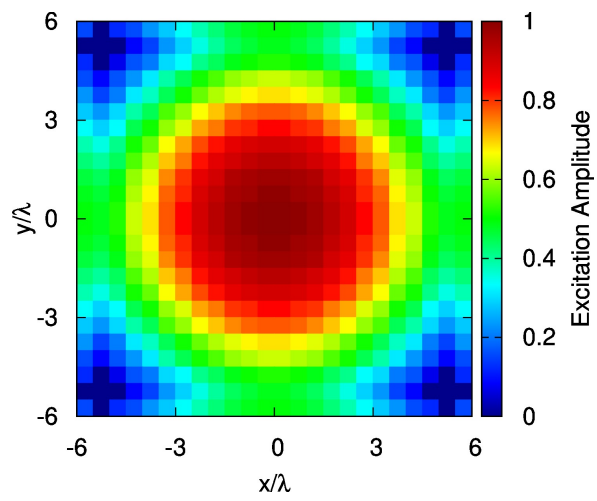


Fig. 8 - N. Anselmi *et al.*, “A Self-Replicating Single-Shape Tiling Technique ...”



(a)



(b)

Fig. 9 - N. Anselmi *et al.*, “A Self-Replicating Single-Shape Tiling Technique ...”

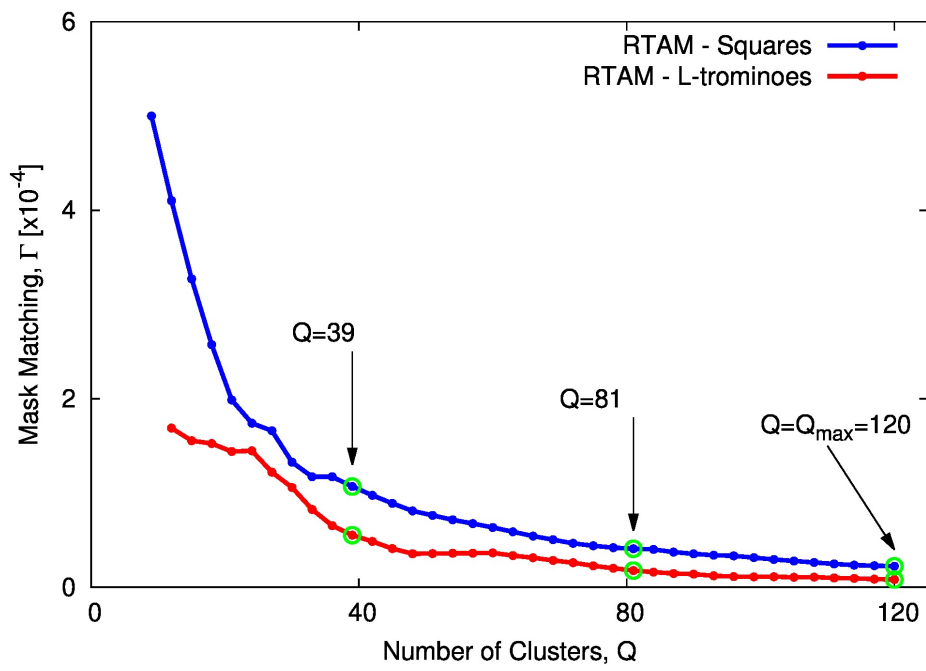


Fig. 10 - N. Anselmi *et al.*, “A Self-Replicating Single-Shape Tiling Technique ...”

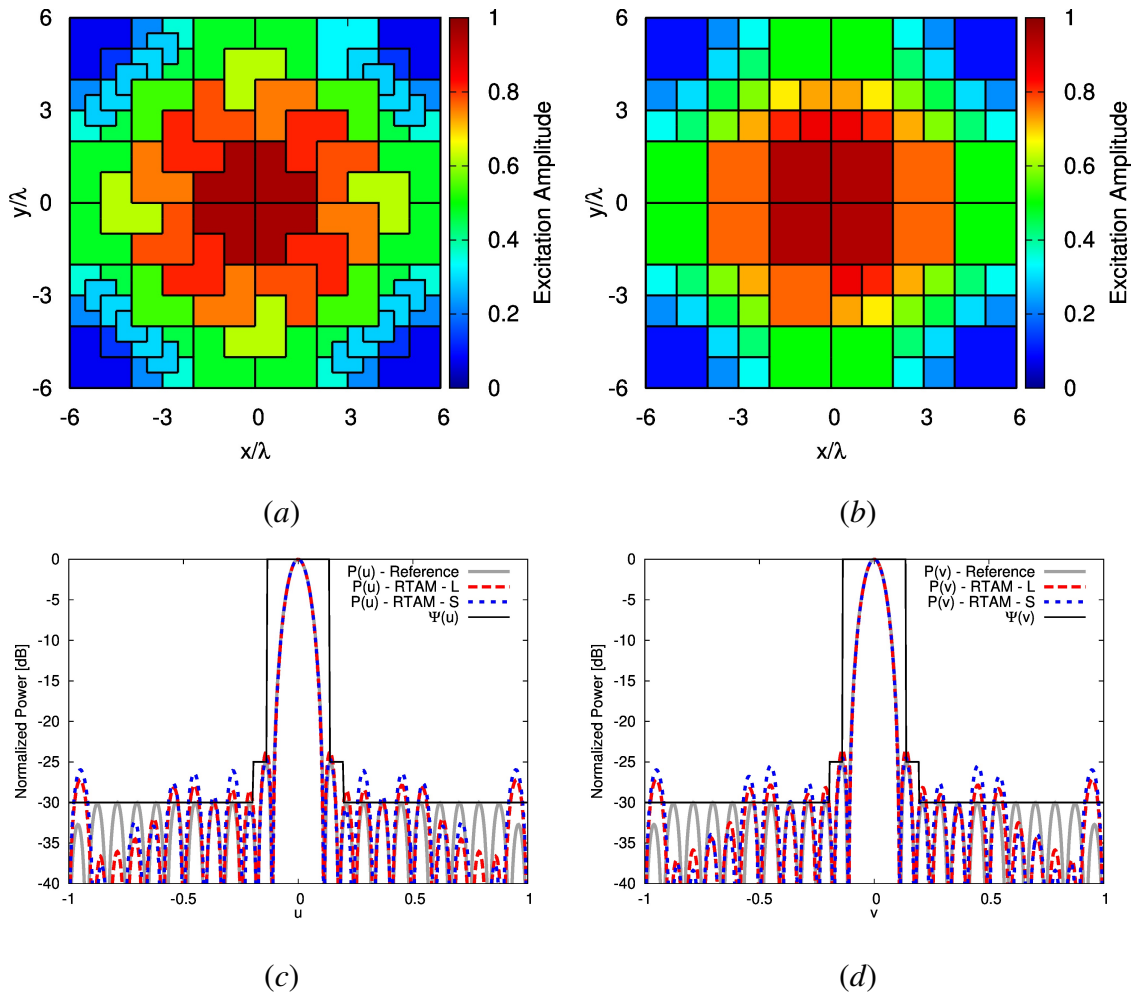
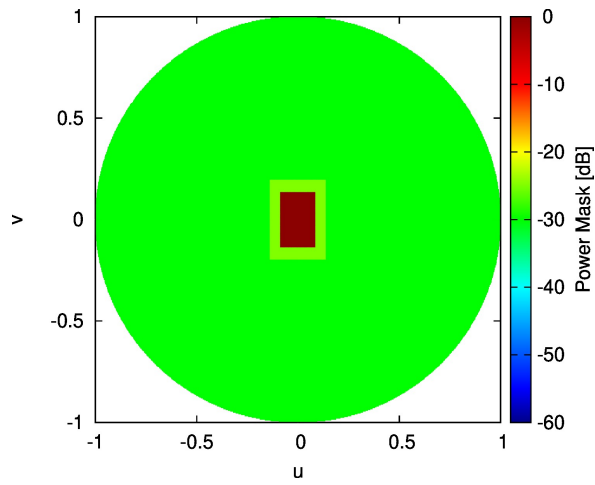
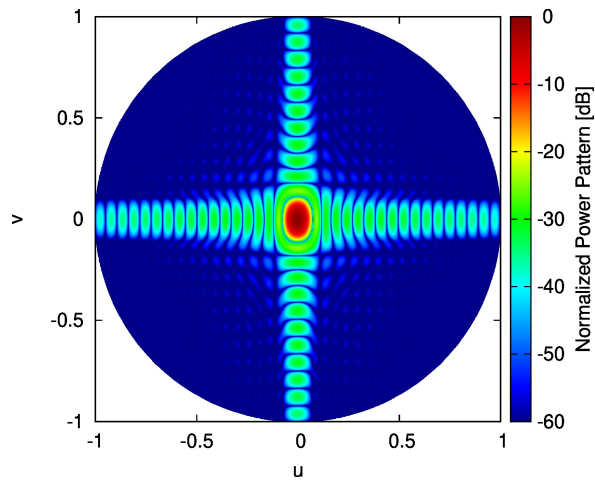


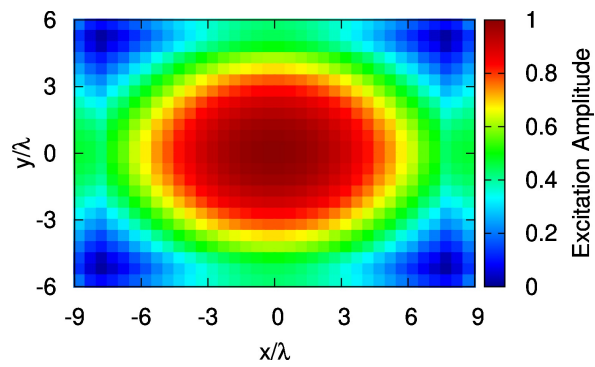
Fig. 11 - N. Anselmi *et al.*, “A Self-Replicating Single-Shape Tiling Technique ...”



(a)



(b)



(c)

Fig. 12 - N. Anselmi *et al.*, “A Self-Replicating Single-Shape Tiling Technique ...”

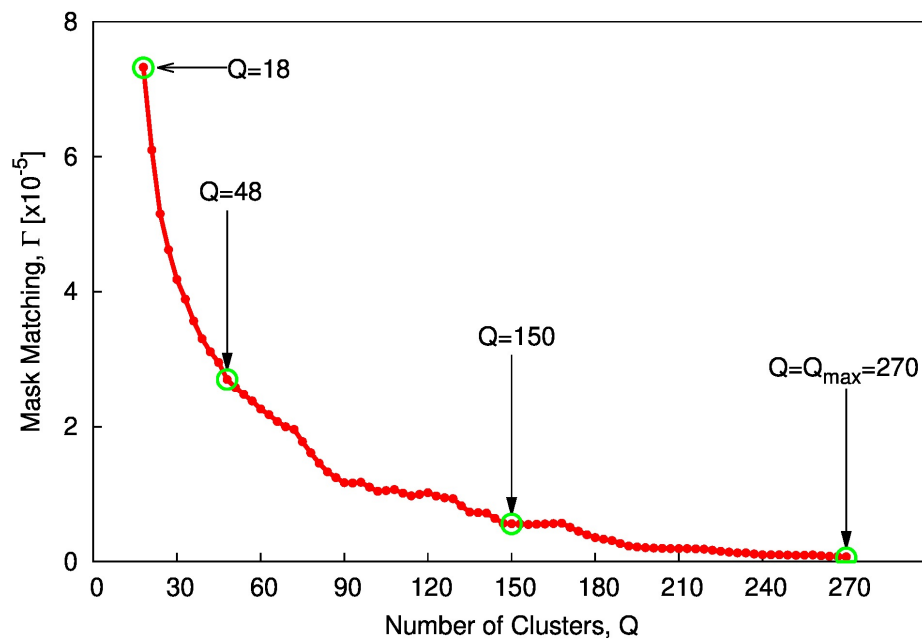


Fig. 13 - N. Anselmi *et al.*, “A Self-Replicating Single-Shape Tiling Technique ...”

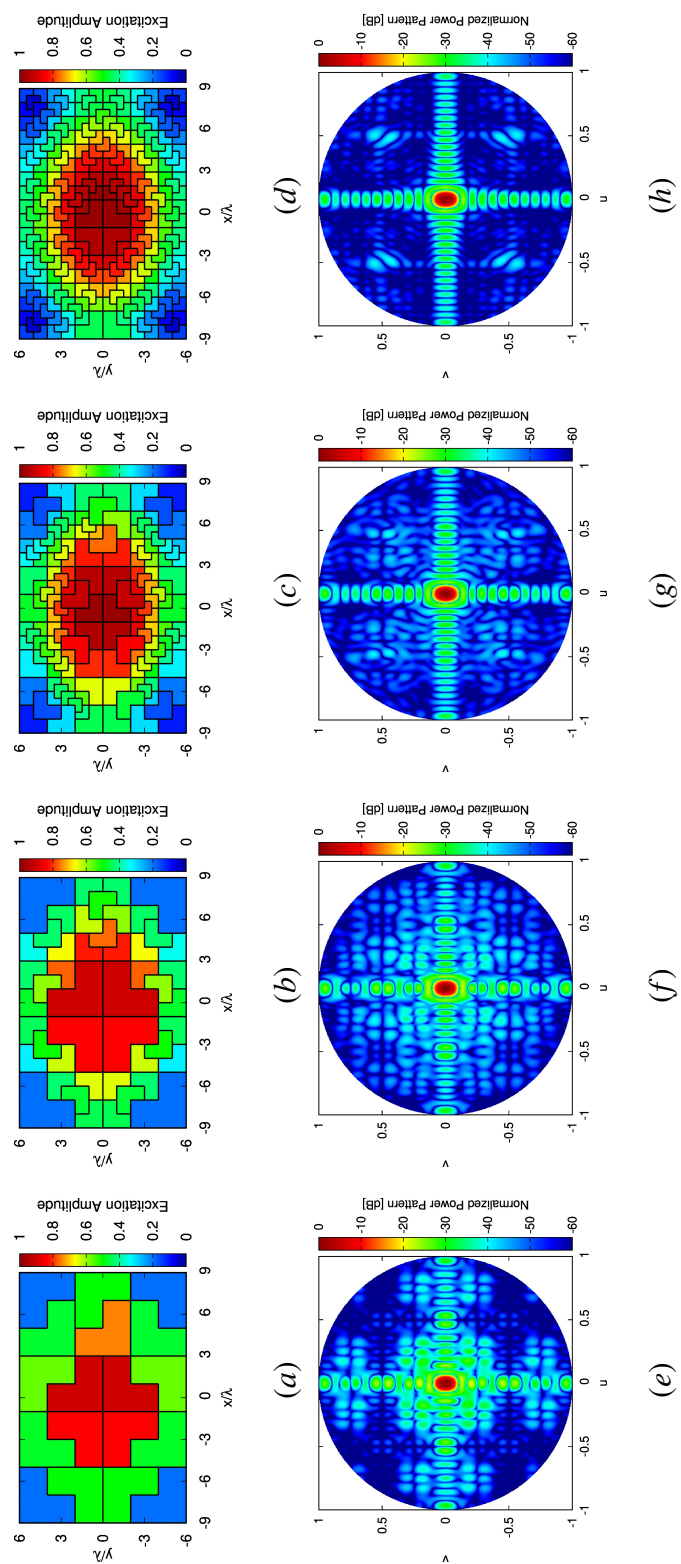
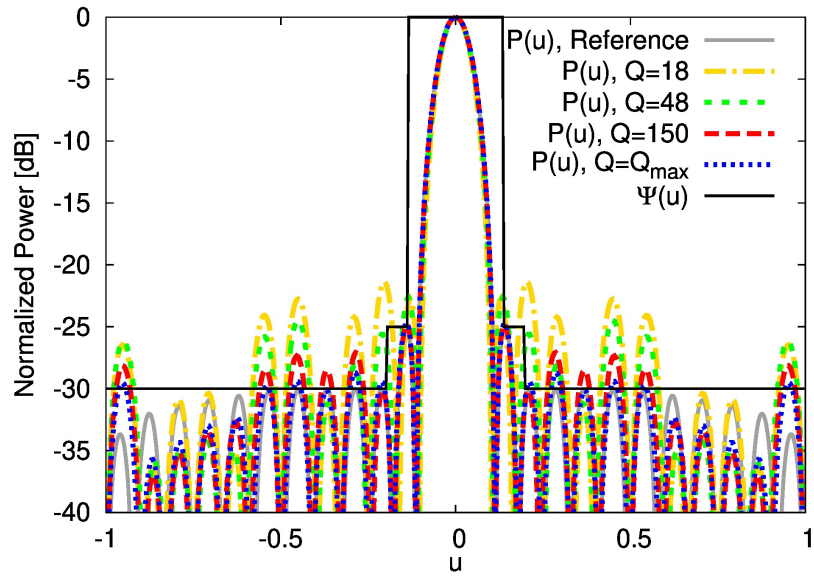
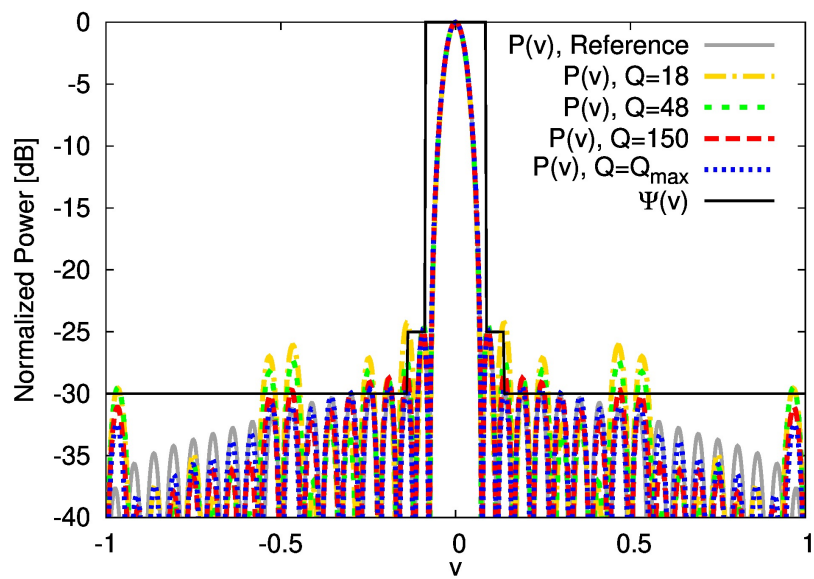


Fig. 14 - N. Anselmi *et al.*, “A Self-Replicating Single-Shape Tiling Technique ...”



(a)



(b)

Fig. 15 - N. Anselmi *et al.*, "A Self-Replicating Single-Shape Tiling Technique ..."

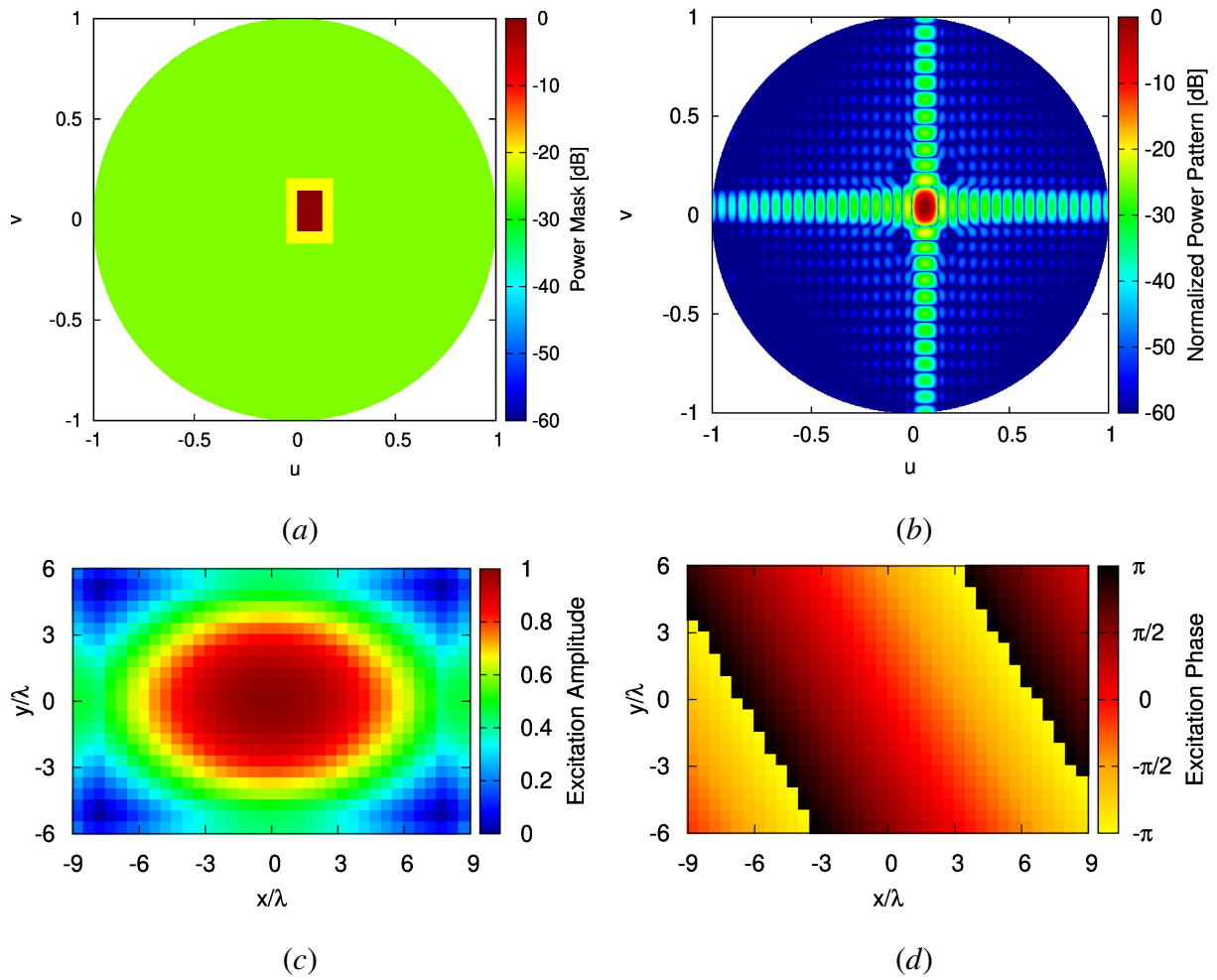


Fig. 16 - N. Anselmi *et al.*, “A Self-Replicating Single-Shape Tiling Technique ...”

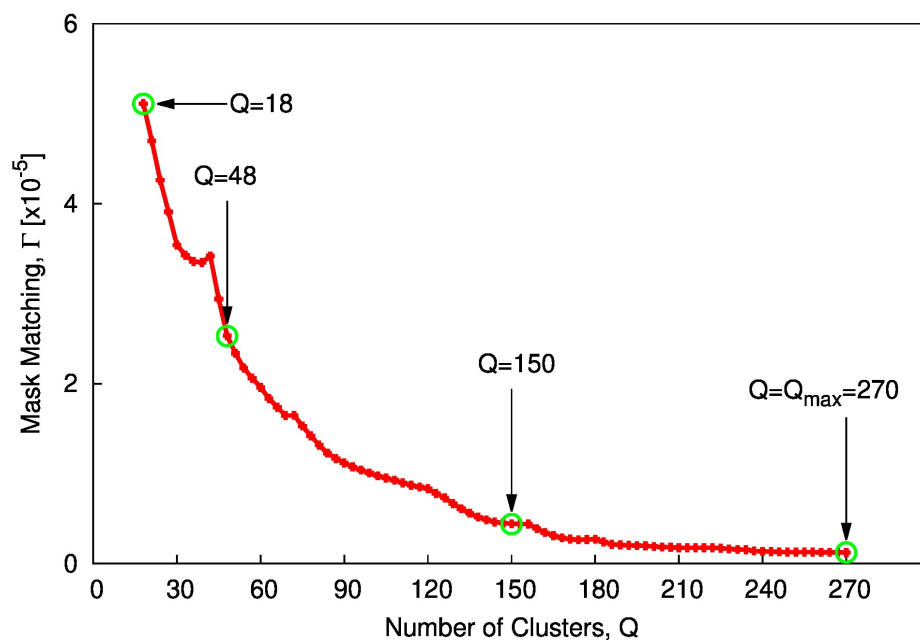


Fig. 17 - N. Anselmi *et al.*, “A Self-Replicating Single-Shape Tiling Technique ...”

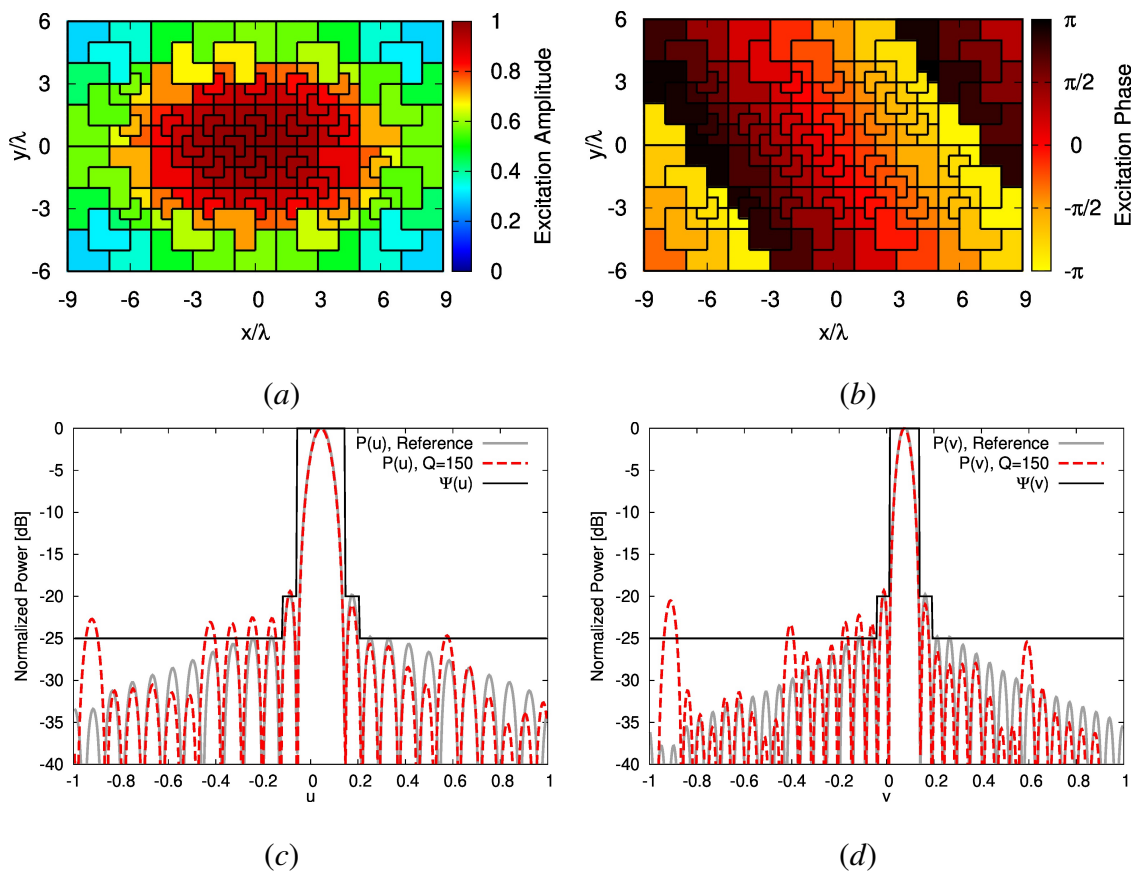


Fig. 18 - N. Anselmi *et al.*, “A Self-Replicating Single-Shape Tiling Technique ...”

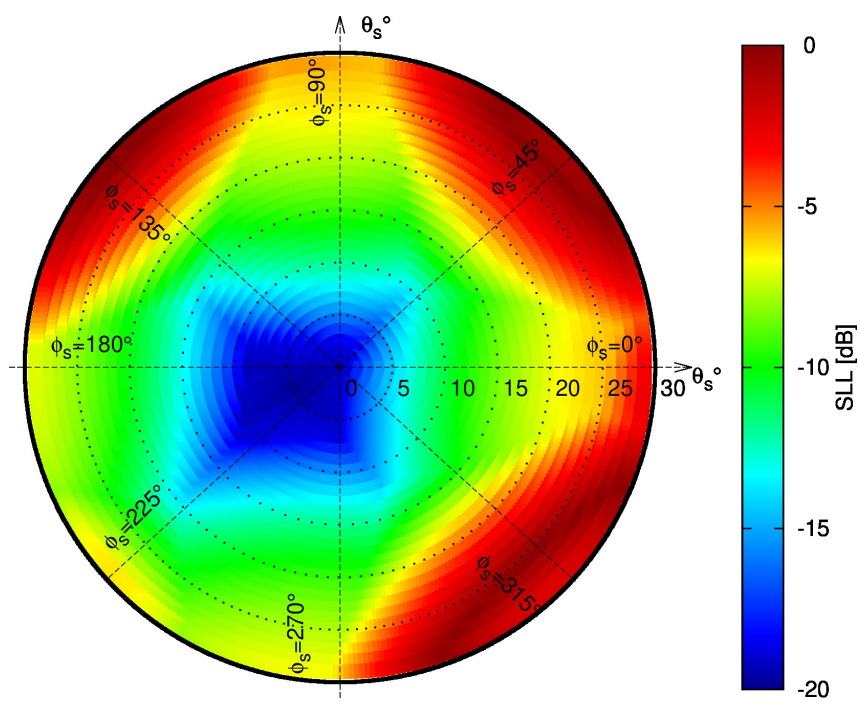


Fig. 19 - N. Anselmi *et al.*, “A Self-Replicating Single-Shape Tiling Technique ...”

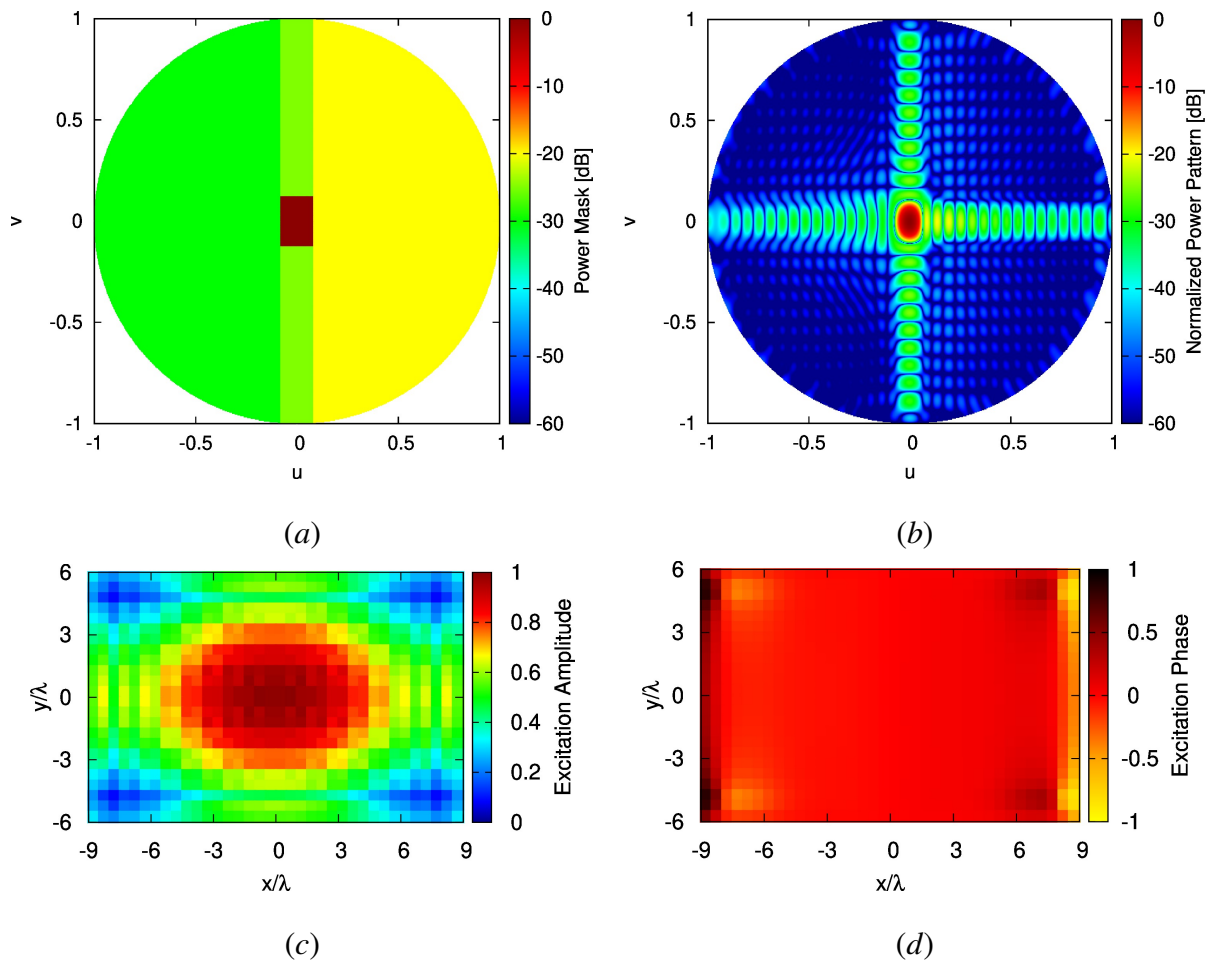


Fig. 20 - N. Anselmi *et al.*, “A Self-Replicating Single-Shape Tiling Technique ...”

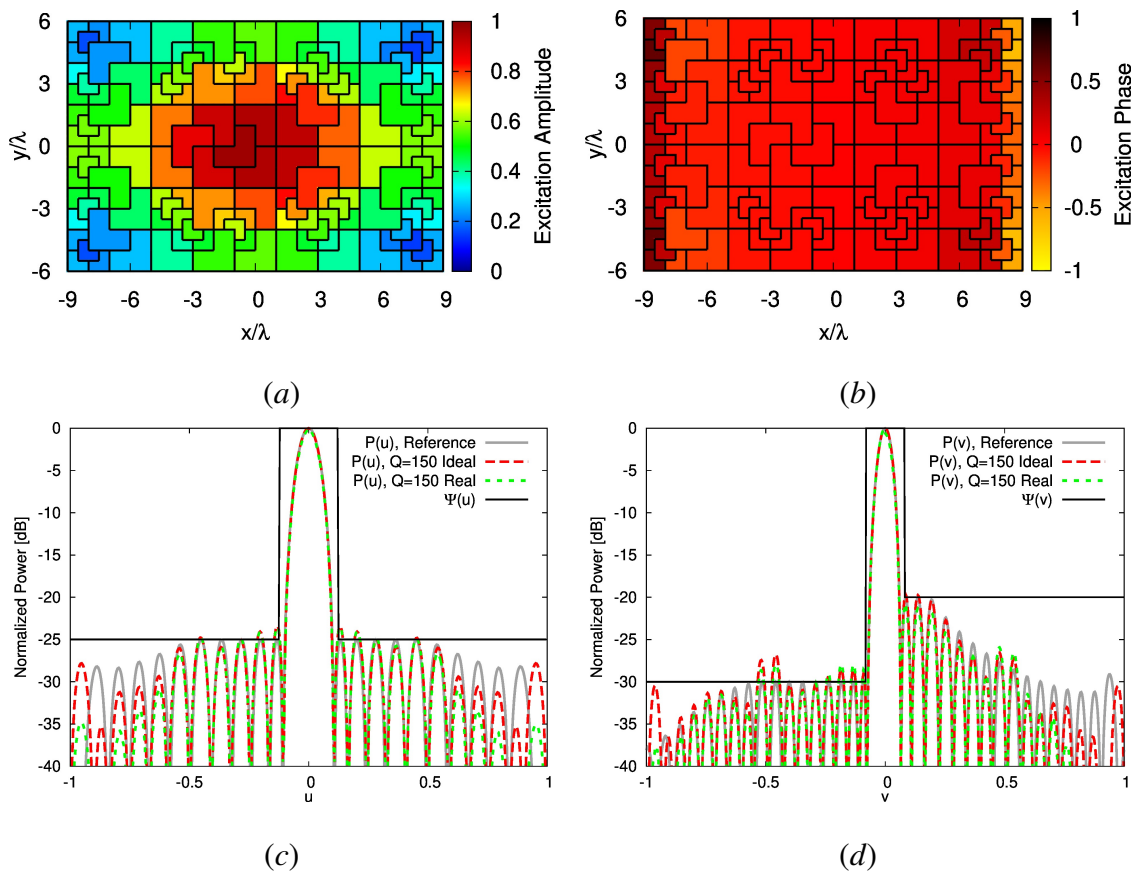
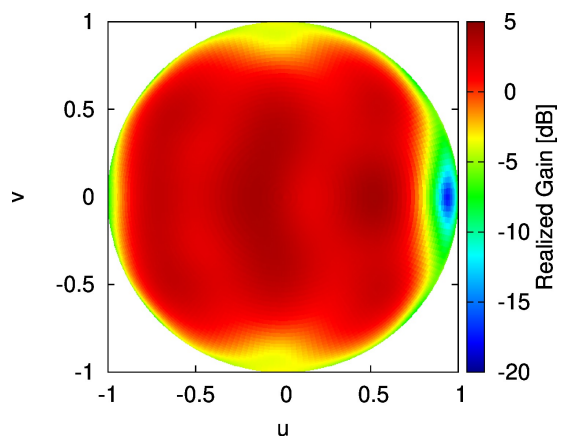
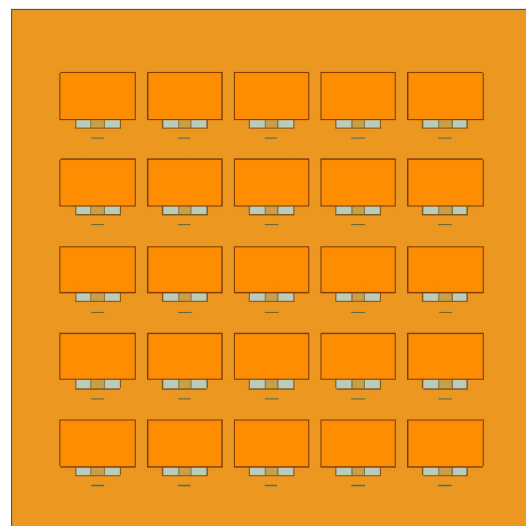


Fig. 21 - N. Anselmi *et al.*, “A Self-Replicating Single-Shape Tiling Technique ...”



(a)



(b)

Fig. 22 - N. Anselmi *et al.*, “A Self-Replicating Single-Shape Tiling Technique ...”

		\widehat{N}							
		2	3	4	5	6	7	8	9
\widehat{M}	2	0	2	0	0	4	0	0	8
	3	2	0	4	0	8	0	16	0
	4	0	4	0	0	18	0	0	88
	5	0	0	0	0	72	0	0	384
	6	4	8	18	72	162	520	1514	4312
	7	0	0	0	0	520	0	0	2.27×10^4
	8	0	16	0	0	1514	0	0	2.04×10^5
	9	8	0	88	384	4312	2.27×10^4	2.04×10^5	1.19×10^6

Tab. I - N. Anselmi *et al.*, “A Self-Replicating Single-Shape Tiling Technique ...”

	Q	Γ	SLL	D	$HPBW_{az}$	$HPBW_{el}$
	-	-	[dB]	[dB]	[deg]	[deg]
Reference	576	7.01×10^{-9}	-24.99	31.58	5.12	5.11
L -trominoes	39	5.53×10^{-5}	-19.31	31.65	4.97	4.97
Squares	39	1.07×10^{-4}	-22.55	31.61	5.02	5.02
L -trominoes	81	1.77×10^{-5}	-23.54	31.60	5.05	5.05
Squares	81	4.08×10^{-5}	-24.49	31.59	5.06	5.07
L -trominoes	120	8.11×10^{-6}	-24.17	31.60	5.08	5.08
Squares	120	2.23×10^{-5}	-24.10	31.58	5.09	5.08

Tab. II - N. Anselmi *et al.*, “A Self-Replicating Single-Shape Tiling Technique ...”

	Q	Γ	SLL	D	$HPBW_{az}$	$HPBW_{el}$
	-	-	[dB]	[dB]	[deg]	[deg]
Reference	864	3.39×10^{-10}	-25.00	33.34	3.39	5.13
<i>RTA</i>	18	7.33×10^{-5}	-21.33	33.46	3.34	4.78
<i>RTA</i>	48	2.58×10^{-5}	-22.63	33.39	3.37	4.95
<i>RTA</i>	150	5.63×10^{-5}	-24.78	33.35	3.38	5.08
<i>RTA</i>	270	7.17×10^{-6}	-24.70	33.35	3.39	5.11

Tab. III - N. Anselmi *et al.*, “A Self-Replicating Single-Shape Tiling Technique ...”

	Q	Γ	SLL	D	$HPBW_{az}$	$HPBW_{el}$
	-	-	[dB]	[dB]	[deg]	[deg]
Reference	864	3.99×10^{-9}	-20.00	33.81	3.18	4.78
<i>RTA</i>	18	7.73×10^{-4}	-12.57	32.70	3.11	4.53
<i>RTA</i>	48	2.85×10^{-4}	-15.91	33.10	3.18	4.65
<i>RTA</i>	150	2.33×10^{-5}	-19.30	33.53	3.18	4.76
<i>RTA</i>	270	1.52×10^{-6}	-19.71	33.71	3.18	4.77

Tab. IV - N. Anselmi *et al.*, “A Self-Replicating Single-Shape Tiling Technique ...”

	Q	Γ	SLL	D	$HPBW_{az}$	$HPBW_{el}$
	-	-	[dB]	[dB]	[deg]	[deg]
Reference - Ideal	864	1.70×10^{-9}	-20.00	33.57	3.25	4.90
Reference - Real	864	1.92×10^{-7}	-21.10	33.85	3.07	4.65
<i>RTA</i> - Ideal	18	5.12×10^{-5}	-20.00	33.57	3.20	4.65
<i>RTA</i> - Real	18	5.24×10^{-5}	-19.97	34.04	3.02	4.43
<i>RTA</i> - Ideal	48	2.53×10^{-5}	-19.12	33.67	3.20	4.76
<i>RTA</i> - Real	48	2.46×10^{-5}	-20.16	33.97	3.03	4.53
<i>RTA</i> - Ideal	150	4.44×10^{-6}	-19.68	33.61	3.22	4.86
<i>RTA</i> - Real	150	3.77×10^{-6}	-20.72	33.90	3.05	4.61
<i>RTA</i> - Ideal	270	1.25×10^{-6}	-19.94	33.60	3.24	4.88
<i>RTA</i> - Real	270	1.74×10^{-6}	-20.98	33.86	3.06	4.63

Tab. V - N. Anselmi *et al.*, “A Self-Replicating Single-Shape Tiling Technique ...”